EUROFUSION WPMST1-PR(16) 15565

D Vezinet et al.

Non-monotonic growth rates of sawtooth precursors evidenced with a new method on ASDEX Upgrade

Preprint of Paper to be submitted for publication in Nuclear Fusion

This work has been carried out within the framework of the EUROfusion Consortium and has received funding from the Euratom research and training programme 2014-2018 under grant agreement No 633053. The views and opinions expressed herein do not necessarily reflect those of the European Commission.

Non-monotonic growth rates of sawtooth precursors evidenced with a new method on ASDEX Upgrade

D Vezinet[1]‡, V Igochine[1], M Weiland[1], Q Yu[1], A Gude[1], D Meshcheriakov[1], M. Sertoli[1], the Asdex Upgrade Team and the EUROfusion MST1 Team[2]

[1] Max Planck Institute for Plasma Physics, Boltzmannstr. 2, 85748 Garching, Germany
[2] see http://www.euro-fusionscipub.org/mst1

E-mail: didier.vezinet@ipp.mpg.de, didier.vezinet@gmail.com

Abstract. This paper describes a new method to derive, from Soft X-Ray (SXR) tomography, robust estimates of the core displacement, growth rate and frequency of a 1/1 sawtooth crash precursor. The method is valid for very peaked Soft X-Ray profiles and is robust against both the inversion algorithm and the presence of tungsten in a rotating plasma. Three typical ASDEX Upgrade crashes are then analysed. In all cases a postcursor is observed, suggesting incomplete reconnection. Despite different dynamics, in all three cases the growth rate of the core displacement shows similar features. First, it is not constant, supporting the idea of non-linear growth. Second, it can be divided into clearly identified phases with quasi-constant growth rates, suggesting sudden change of growth regime rather than smooth transitions. Third, its evolution is non-monotonic, with phases of accelerated growth followed by damped phases. This damping is interpreted for two cases respectively as an effect of fast ions and of mode coupling, based on the result of a MHD simulation. The mode frequency is observed in all cases to be closely related to the plasma bulk rotation profile, with little or no visible effect of the electron diamagnetic drift frequency. The onset criterion could not be clearly identified and it is shown that the role of the pressure gradient is not as expected from a naive extrapolation of the linear stability theory.

PACS numbers: 52.30.Cv, 52.70
Tokamak, MHD, Soft X-Ray tomography, sawtooth crash precursor Submitted to: *Nucl. Fusion*

‡ Present address: Max Planck Institute for Plasma Physics, Div. E1, room L6/190, Boltzmannstr. 2, 85748 Garching, Germany

Contents

1. Introduction

In a typical tokamak plasma, the electron temperature and density profiles are peaked on the magnetic axis and monotonically decreasing to the plasma edge. Plasma performance is determined mostly by the maximum value and the gradients of these profiles. In 1974, it was discovered that a quasi-periodic relaxation phenomenon could flatten these profiles in a region around the plasma core [1]. It was visible on the time traces of Soft X-Ray (SXR) signals in the form of a sawtooth-like oscillation and the community labelled it "sawtooth crashes" or "internal disruptions" [2].

The profile relaxation associated to sawtooth crashes, which were later confirmed to be quite common on tokamaks, typically affects a central region delimited by the mixing radius, which is slightly larger than the q=1 surface (when it exists), where q is the safety factor (the "winding" of the magnetic field lines), typically monotonically increasing from the center to the edge. This region can include up to half the total plasma volume, as expected on ITER [3], thus periodically affecting the plasma perfomance. Moreover, sawtooth crashes can trigger other dangerous instabilities, like Neo-classical Tearing Modes (NTMs) that degrade the plasma confinement by flattening the current profile [4, 5, 6]. Consequently, significant efforts have been put into understanding this phenomenon over the past decades. Sawtooth crashes are typically preceded by a displacement of the old core of the plasma [1, 7, 8, 9], shortly before the crash itself. This displacement results from a (m/n) = (1/1) MHD instability refered to as a "sawtooth crash precursor".

The exact processes behind sawtooth crashes and precursors remain unclear. Several models were proposed over the years. Some models proposed for example a fast change in the magnetic topology via full magnetic reconnection of a resistive m/n = 1/1 mode [8, 10, 11], the formation of plasmoids in the tearing-unstable reconnection layer that then coalesce into a secondary island [12], or a transition from quasiperiodicity to stochasticity in the plasma center [13, 14, 15].

All these approaches have been confronted to experimental measurements that contradict or validate them. One of the difficulties with sawtooth crashes lies in the apparent diversity of the experimental phenomenology and on the diagnostics limitations. This diversity, the measurement uncertainties, and the difficulty to identify a universal sawtooth crash model explain why the crash nature, its onset mechanism and its driving process still escape consensus to this day.

Part of the answer could lie in the possibility that several processes are indeed possible, and that different plasma conditions make one or another dominant at a given time, possibly with very subtle thresholds. This could reconcile antagonist observations from different tokamaks and explain why the sawtooth precursor characteristics "can vary significantly even from one sawtooth event to the next, while the basic discharge parameters have hardly changed" [16].

With this diversity in mind, we propose an approach consisting in a systematic quantitative characterisation of a large number of sawtooth crash precursors corresponding to various plasma configurations. This way, it is hoped that general trends can be identified robustly. This requires a clearly defined method and its systematic application to a large database. Such characterisation of sawtooth crash precursors can be achieved via SXR tomography, which can give ac-

cess to an estimate of the core displacement.

This paper is the first step of this approach: it presents and details a robust method and evaluates its reliability in realistic conditions. It then uses this method to underline, in 3 typical cases, that the precursor growth rate does not necessarily undergo a monotonic increase up to the crash. Possible explanations are discussed in each case. Results drawn from a larger database will be treated in a separate article.

This article is structured as follows: section 2 shows that the displacement and growth rate of 1/1 modes can be robustly retrieved by SXR tomography, provided that the SXR profile is peaked and that the growth rate is not larger than the mode frequency. Some key parameters used to characterise sawtooth precursors and allow direct comparisons are quantitatively defined in section 3. In section 4 this method is applied to three typical but different precursors. It is shown that the growth rate behaviour is not monotonic and can be approximated as a set of well-identified phases with quasi-constant growth rate. Also, all three cases show postcursor oscillations compatible with incomplete reconnection, itself compatible with both plasmoids [12] and stochasticity interpretations [15].

This work is the continuation of an effort initiated in [17], with an improved method, stronger justfication, more technical details and more in-depth analysis of particular cases.

2. Deriving the core displacement from SXR tomography for peaked profiles

Several diagnostics can be used to monitor a sawtooth crash precursor, and some interesting results have been produced thanks to ECE [18, 19, 20, 21] or 2D ECE imaging [18, 22, 23], thanks to reflectometry via 2D density rotational tomography [24], or thanks to polarimetric measurements, which give access to line-integrated electron density and perturbed magnetic field [9], from which central current density can be derived [25]. Magnetic measurements or interferometry can also be used.

Nevertheless, all these diagnostics have limitations. In particular, the electron temperature, which gives the most direct access to magnetic structures (due to fast heat conduction along field lines), is not always accessible up to the plasma center (due to cut-off), automatically excluding shots with too high density. As for 2D ECE, it only reveals its full potential when the displaced core passes through its viewing window, which limits the accessible cases. Core polarimetric measurements are not always available and, like 1D ECE and interferometry, they miss the bidimensional dynamics of precursors. Rotational tomography from reflectometer data was not possible on the presented AUG discharges. Finally, magnetic measurements are located at the plasma edge, so core mode signals have to be corrected for mirror currents [26], toroidal mode coupling [27, 28] and decay [21].

The use of SXR tomography, already advocated for precursor studies in [2, 8], is thus complementary to the previous diagnostics, thanks to its 2D nature and the fact it is virtually always available. In particular, the SXR diagnostics of ASDEX Upgrade, which benefits from excellent geometrical coverage and relative calibration, is a very good option for a systematic study in various plasma conditions since it catches the 2D structure of 1/1 modes with a good time resolution (up to 2 MHz).

However, in tokamaks where tungsten is used as a plasma facing material, the plasma gets polluted by small concentrations of W which, due to the strong radiative properties of this element [29], are sufficient to radiate large amounts of energy out of the plasma core. In particular, the SXR radiation on ASDEX Upgrade is typically dominated by W. Additionaly, the use of NBI heating, which transfers a lot of momentum to the plasma (resulting in toroidal velocities up to 100-200 km/s in AUG), and thus accumulates W on the Low Field Side (LFS) [30, 31], or of off-axis ICRH, which accumulates W on the High Field Side (HFS) [32, 33, 34], mean that SXR emissivity can be poloidally asymmetric and can no longer be considered as a flux-surface quantity. Hence, particular care must be taken as the SXR maximum does not necessarily match the magnetic axis.

In the following, the SXR diagostics of ASDEX Upgrade and the general principles of tomography are briefly introduced, focusing on the main improvements recently implemented. It is then shown that, for peaked SXR profiles, SXR tomography can be used to robustly trace the trajectory of the SXR maximum independently of the inversion algorithm used. Then, it is shown that this trajectory is a robust estimate of the core trajectory despite a shift between the SXR maximum and the plasma center due to the presence of W in a rotating plasma. Finally, a robust definition is proposed for the displacement that takes into account experimental difficulties.

2.1. The SXR diagnostics of ASDEX Upgrade and tomography

The SXR diagnostics of ASDEX Upgrade [35, 36] has 12 camera heads distributed around the poloidal cross-section, as shown in Fig 1 (a,b). Each camera comprises between 9 and 22 semiconductor diodes placed behind a common aperture and Be filter cutting off the low energy photons to focus on the core plasma, resulting in a total of 182 usable Lines Of Sight (LOS)§. The number of cameras and their poloidal distribution allow for a good geometrical coverage, a necessity for accurate tomographic inversions. We used the geometry of the 2014 campaign. All signals in this article are downsampled to 200 kHz.

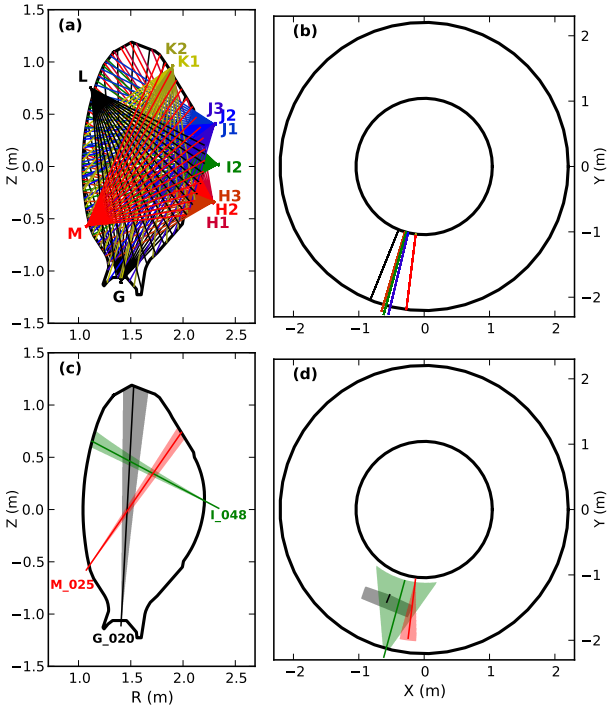

Figure 1: Geometry of the SXR diagnostics on AUG represented as LOS in (a) poloidal and (b) horizontal projections, as well as selected VOS in (c) poloidal and (d) horizontal projections

The diodes provide a signal corresponding to the total power received on their active surface, spectrally filtered by η, which includes the Be filter and the diodes reponse function‡. Signal $f_i(t_n)$ issued at time step t_n by diode number i is:

$$f_i(t_n) = \int\int\int_{VOS}\int\int_{4\pi} \epsilon^{\eta}(\underline{x}, t_n)\Omega_i(\underline{x})d^2\Omega d^3V$$

§ excluding camera F which is at a different toroidal position and camera heads I1 and I3 which have different Be filters

‡ which depends on the diode thickness, the type of semiconductor junction and the bias voltage used

where $\epsilon^{\eta}(t_n) = \int_0^{\infty} \eta(E)\epsilon(\underline{x}, E, t_n)dE$ is the plasma emissivity at time t_n at position $\underline{x}$, spectrally filtered by the diagnostic response η. The solid angle subtended by the detector-aperture system as seen from point $\underline{x}$ in the plasma is $\Omega_i(\underline{x})$ for detector i. The spatial integration is done over the plasma volume viewed by the detector through its associated apertures, also called Volume of Sight (VOS), some of which appear in Fig. 1 (c,d). Computing these VOS is a demanding task, and is one of the main improvements implemented for this article.

At a given time, the signals from all detectors provide a set of projections of the (unknown) emissivity. These are a set of Fredholm integral equations of the first kind, which are ill-posed by nature [37]. Additionally, $\epsilon^{\eta}(t_n)$ is a continuous scalar field with an infinite number of unknowns (but only a limited number of equations, one per detector), the problem is thus also under-determined. To reduce this under-determinedness, the solution is approximated by its discretization over a set of basis functions in physical space $\epsilon^{\eta}(t_n) \approx \sum_{j=1}^{N} c_j(t_n)\epsilon_j^{\eta}$ weighted by coefficients $c_j(t_n)$ (the unknowns). Several types of basis functions are possible [38], the simplest of which being pixels. In our case, the basis functions are a set of bivariate b-splines of any degree between 0 (pixels) and 2, and supported by a variable mesh grid (larger near the edge where the emissivity is smoother and weaker, to minimise the computation time), as seen in Fig 2. The use of advanced basis functions is another significant improvement implemented for this article.

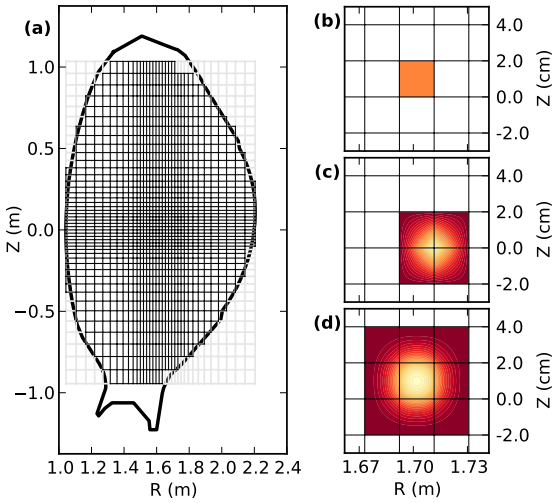

Figure 2: (a) Illustration of the variable size mesh and basis functions of degree (b) 0, (c) 1 and (d) 2

The contribution (i.e. volume integral) of each basis function to each detector measurements is stored in the geometry matrix $\underline{\underline{T}}$. Since SXR diagnostics

used for tomography are especially designed to create narrow viewing volumes (in the poloidal direction, to maximise poloidal resolution), it is tempting to approximate the VOS as a Line of Sight (LOS), thus simplifying the computation of $\underline{\underline{T}}$, which becomes a set of 1D, instead of 3D, integrals. Indeed, the fact that the SXR emissivity is expected to be quasi-constant in the toroidal direction compensates the fact that the VOS is usually *not* narrow in the toroidal direction (to maximise the signal / noise ratio). Moreover, if one choses a LOS, directed by vector $\underline{k}$, inside the VOS, the integral of $\Omega_i(\underline{x})$ over any surface perpendicular to this LOS is a constant quantity called the *etendue* $E_i(\underline{k})$. Using this approximation amounts to writing, with $S(\underline{k})$ being any surface perpendicular to $\underline{k}$:

$$\begin{cases} f_i(t_n) \approx f_i^{\underline{k}}(t_n) & = E_i(\underline{k}) \int_{LOS} \epsilon^\eta(\underline{x}, t_n) dl \\ E_i(\underline{k}) & = \int\int_{S(\underline{k})} \int\int_{4\pi} \Omega_i(\underline{x}) d^2\Omega d^2 S \end{cases}$$

Even though this LOS description is quite common and is often a reasonable first-order approximation, it remains inferior in precision to a full-3D description (VOS) [36, 39]. This is particularly true when the emissivity field has a non-negligible second derivative in a plane perpendicular to the LOS (i.e.: on the planes used to compute the etendue), as it happens for very peaked and very hollow profiles or profiles with narrow structures (small islands), all quite common in tungsten-contaminated plasmas. Hence, in order to suppress this source of inaccuracy, we implemented a full 3D computation of $\underline{\underline{T}}$. Indeed, the ill-posedness of the problem means that inversions are highly sensitive to small errors in the equations and to noise. In addition to this effort, a Phillips-Tikhonov regularisation is also used [40, 41]. Hence, the discretised solution vector $\underline{\epsilon}^\eta(t_n) = (c_1 ... c_N)$, defined by the values of the basis functions coefficients at time t_n is found by minimising the functional $\Phi_{t_n}(\underline{\epsilon}^\eta)$ such that:

$$\Phi_{t_n}(\underline{\epsilon}^\eta) = \|\underline{\underline{T}}\underline{\epsilon}^\eta - \underline{f}(t_n)\|_2^2 + \alpha H(\underline{\epsilon}^\eta)$$

where α is a positive scalar called the regularisation parameter that sets the trade-off between fitting to the measurements and regularity, and H is the chosen regularisation functional. The choice of α can be done using several algorithms [37, 42, 43], and the choice of H determines the kind of bias we want to introduce [44, 45] (e.g.: smaller absolute value, gradient, curvature...). More information about tomography diagnostics and inversions can be found in [46, 47].

Details of the implemented techniques will be discussed in depth in a future publication [48]. In the present article, three different types of regularisation, with different basis functions, have been benchmarked to assess the robustness of our observations.

2.2. Robustness versus regularisation methods

The difficulty with tomography is to determine which of the reconstruction features are physical, and which are artefacts. We are interested here in the position of the SXR profile maximum, which also means that we are *not* interested in: the SXR profile in its entirety, the absolute value of the SXR maximum (at most we may be interested in its relative evolution), or the level of poloidal asymmetry due to tungsten. All we need is a robust trajectory of the SXR maximum, and this is best achieved with very peaked SXR profiles, for at least two reasons:

- the SXR maximum is unambiguously identified.
- the SXR maximum position is a well-constrained aspect of the inversion, because small shifts induce large changes in central channels signal.

Hence, we decided, as a first step of a long-term effort, to focus primarily on very peaked SXR profiles which are common in AUG since the introduction of tungsten as a plasma facing material. Thus, by limiting our analysis to such cases we significantly limit the risks of ambiguous maximum location while still accessing a large number and diversity of sawtooth crashes, especially since a peaked SXR profile in a W-contaminated plasma does not necessarily mean a peaked electron temperature profile.

To illustrate the robustness of the SXR maximum position, 2D reconstructions of experimental data were done using the following basis functions and regularisation functionals:

- b-splines of degree 0 (pixels) with discrete formulation of the Fisher functional [44] (D1FI)
- b-splines of degree 1 with exact formulation of 1st order linear functional [44] (D1N2)
- b-splines of degree 2 with exact formulation of 2nd order linear functional [44] (D2N2)

Notice that all regularisations are isotropic. Indeed, anisotropic regularisation - i.e.: greater smoothing in the poloidal than in the radial direction [45, 49, 50] - relies too much on the *unknown* 3D equilibrium and would induce a bias that would be particularly unwelcome for a m/n = 1/1 mode. Finally, all inversions include a positivity constraint ($\epsilon^\eta > 0$) and a boundary constraint at the separatrix (where $\epsilon^\eta \approx 0$).

As can be seen in Fig 3, which shows cuts in the horizontal plane ($Z = 0$) of the reconstructed profiles, the position of the SXR maximum is a quite robust feature that hardly suffers modifications from the choice of regularisation. This is primarily due to the intrinsic qualities of the SXR diagnostics (geometrical

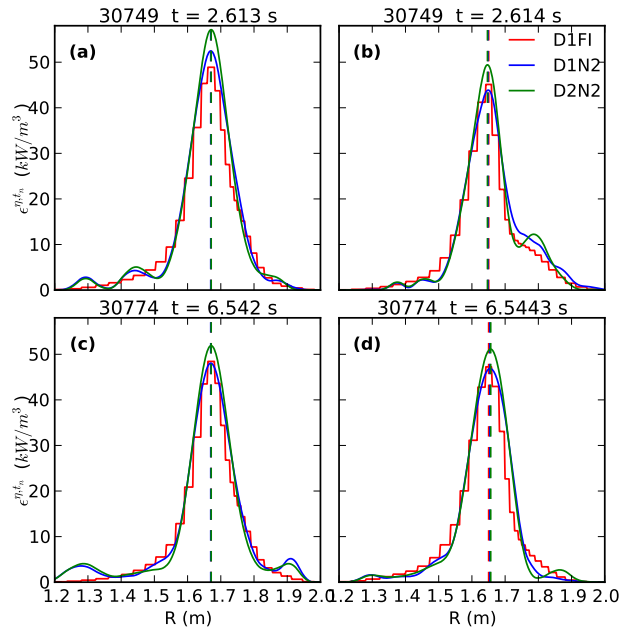

Figure 3: (a-d) Experimental SXR profile reconstructions using in each case D1N2 (1st order linear regularisation with degree 1 b-splines), D2N2 (2nd order linear regularisation with degree 2 b-splines) and D1FI (minimum Fisher regularisation, with pixels). Dashed vertical lines mark the position of the maximum for each inversion.

coverage, signal to noise ratio and relative calibration) and to the choice to limit the analysis to peaked SXR profiles. This robutsness is quantified in table 1 by computing the difference Δ between the positions of the maximum derived from each inversion method and comparing it to the mesh size (2 cm) and to the Full Width at Mid Height ($FWMH$) of the profile:

Table 1: SXR maximum position precision

shot	30749	30749	30774	30774
t (s)	2.613	2.614	6.542	6.5443
$\Delta(D1N2-D2N2)$ (mm)	1.2	1.2	1.2	2.4
$\frac{\Delta(D1N2-D2N2)}{FWMH}$ (%)	0.9	1.4	1.1	2.2
$\Delta(D1FI-D1N2)$ (mm)	1.2	2.4	1.2	3.6
$\frac{\Delta(D1FI-D1N2)}{FWMH}$ (%)	0.9	2.7	1.1	3.4
$\Delta(D1FI-D2N2)$ (mm)	0.0	3.6	0.0	6.0
$\frac{\Delta(D1FI-D2N2)}{FWMH}$ (%)	0.0	4.1	0.0	5.7

These results are representative of this article: the SXR maximum is generally localised within a few millimeters. This sub-mesh precision is made possible in two complementary ways:

- High-order b-splines allow more accurate reconstructions since the error scales as h^p, where h is the mesh size (normalized < 1) and p is the degree.
- The position of the maximum is defined as the center of mass $\underline{M}$ of the top 5 % of the profile:

$$\underline{M}(t_n) = \frac{\int\int_{S(\epsilon>\epsilon_{Lim})} \underline{x}\epsilon^{\eta,t_n} d^2S}{\int\int_{S(\epsilon>\epsilon_{Lim})} \epsilon^{\eta,t_n} d^2S}$$

where $S(\epsilon > \epsilon_{Lim})$ is the surface on which the emissivity is greater than $\epsilon_{Lim} = 0.95 \max(\epsilon)$. This is particularly useful for pixel basis functions but hardly changes the result for higher-order basis functions, at most making it more robust versus noise.

By performing inversions every 5 microsecond during the whole lifetime of the precursor, we can plot in Fig 4 the trajectory of $\underline{M}$ in the poloidal plane. Again, the same two examples as in Fig 3 are reconstructed using the same 3 regularisations.

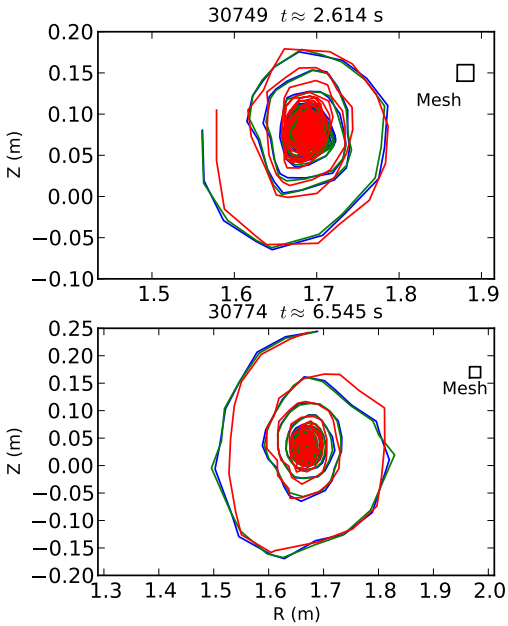

Figure 4: Reconstructions via tomography of the SXR maximum trajectory during two different precursors with 3 regularisations (same color code as in Fig 3)

As expected, the choice of the inversion techniques does not affect significantly the reconstructed trajectory, which is an outward spiral (due to plasma rotation and growing displacement). The general shape and dynamics are pretty robust despite isolated discrepancies.

It is important to keep in mind that this spiral is the trajectory of the SXR maximum, and that there is no guarantee, in a W-polluted rotating plasma, that it matches the plasma core, even for a peaked SXR profile. We will now investigate the relationship between these two objects.

2.3. Robustness versus tungsten and plasma rotation

Since the proposed method uses the SXR maximum as a proxy for estimating the core displacement, we must check that this proxy is relevant despite poloidal asymmetry. This is done for NBI-induced centrifugal force thanks to a numerical tool developed at IPP that simulates the 3D SXR emissivity stemming from a W-contaminated plasma with a rotating (1/1) island [36]. This code uses the 1/1 mode description introduced in [51] and, taking the total impurity density on a given flux surface as an input, computes its 3D redistribution in a rotating non-axisymmetric plasma. In this respect, it is an extension of the 2D redistribution proposed in [30, 31] for an axisymmetric plasma. This advanced tool allows to estimate the behaviour of the SXR maximum with respect to the displaced core trajectory.

However, it must be kept in mind that it is not a transport model in the sense that it does not have dynamic terms (it is fully static) and that it does not include a model for plasma and W redistribution through the X point. Thus, the W density profile is only relevant for small displacements (up to half the radius of the $q = 1$ surface in the following). In Fig 5, the SXR emissivity is shown (filled contours) over the magnetic surfaces (white contours) for two displacement and rotation values. It is a worst-case scenario since the SXR radiation is assumed to be W-only and W is most strongly affected by centrifugal force. The background equilibrium is experimental AUG shot #26355 at $t \approx 2$ s with $T_e(0) \approx 2$ keV.

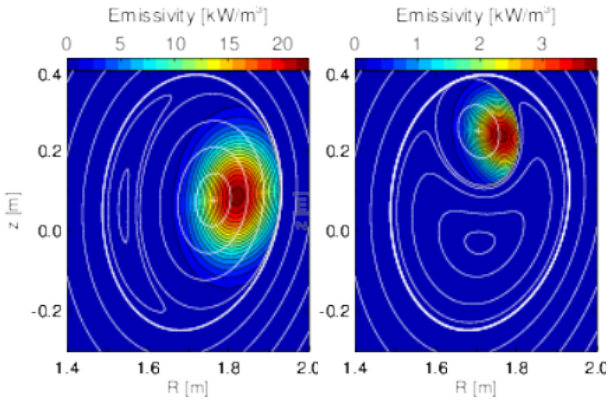

Figure 5: Simulated W-only SXR emissivity from a Porcelli-like 1/1 mode rotating at 15 kHz with displacement 0.09 (left) and 20 kHz, with displacement 0.28 (right). The thick white contour is q=1.

There is a clear shift between the SXR maximum and the displaced core. The main component of this shift is horizontal, as expected, towards the LFS and is due to the centrifugal force. There is also a small vertical component due to the shaping of the perturbed magnetic surfaces (originating from the shaping of the magnetic equilibrium). The SXR maximum is aligned in regions, where the perturbed magnetic surfaces are vertical (because this defines the outermost position of a given flux surface), and in general, this is located at a different height than the displaced core itself.

In Fig 6, both trajectories are plotted over one period for 4 different displacements, with a high mode frequency (20 kHz), to check how the shift varies with the mode phase. The shift, quantified by distance d between the SXR maximum and the displaced core is also plotted versus phase θ for a scan of several cases (varying the frequency and displacement).

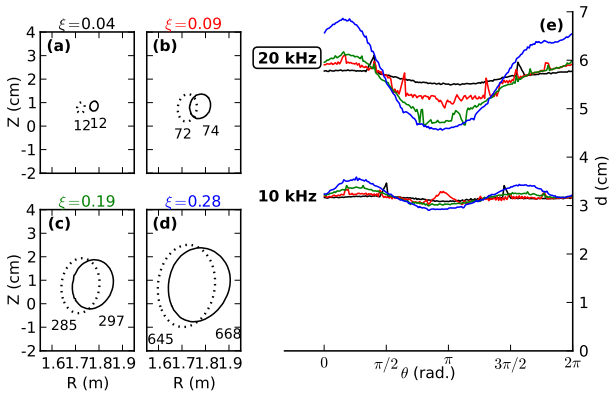

Figure 6: (a-d) Trajectories of the SXR maximum (solid) and displaced core (dotted) for $f = 20$ kHz and various displacement ξ, numbers are the surface (cm^2) of each trajectory (e) Shift d between the SXR maximum and hot core versus the mode phase for various displacements (same colors as in (a-d)) and two mode frequencies.

As expected, higher plasma rotation means larger distance between the SXR maximum and the displaced core. Also, the phase modulates this distance due to the asymmetry scaling: $\epsilon^\eta(\rho, R) \approx \epsilon_0^\eta(\rho) e^{\lambda(\rho)(R^2 - R_{ref}^2)}$ [36], where R and ρ are the major and minor plasma radius. For this Porcelli-based mode description, the trajectory elongation is also slightly reduced. Despite the shift and small distortion, even this worst-case scenario shows that the area spanned by each trajectory during one period is very similar and can be used to define an average radius. The little fluctuations visible on the low-ξ curves are numerical errors of the order of the mesh size.

Although these simulations involve a resistive precursor, we see no reason for the effect to be different with another kind of precursor. As long as the SXR profile is peaked, we think that assuming that its trajectory is a translated (and slightly distorted) version of the core trajectory is a good approximation.

However, these simulations are done with a fixed displacement, while experimental data show a constantly growing displacement such that the trajectory is an outward spiral. Before simulating such growing modes, it is necessary to propose a robust definition of the displacement from such a spiral.

2.4. Defining the displacement

The core displacement ξ has to be approximated by a SXR displacement ξ_{SXR} robustly derived from experimental SXR trajectory§. A naive approach would estimate the distance between the magnetic axis (from equilibrium reconstruction) and the SXR maximum. This is not valid because the center of rotation of the SXR maximum (i.e.: the spiral center) is usually *not* the magnetic axis - as evidenced in Fig 6 (a-d) - due to the rotation-induced asymmetry. For the same reason, and also because a magnetic equilibrium reconstruction, ill-constrained in the center, introduces additional sources of uncertainty, it seems difficult to define the displacement from any flux coordinate.

More generally, methods measuring the absolute distance between the SXR maximum and any fixed point should be avoided because:

- The spiral center is unknown, and experimental data shows that it drifts (slowly compared to the mode frequency, but fast enough - compared to the precursor lifetime - to induce a bias)
- The plasma elongation and shaping introduce additional fluctuations of the measured distance, which are not displacement
- The experimental data and tomography are never perfect, occasional errors introduce fluctuations

Instead, an area-based quantity is more robust, depends less on the plasma elongation and does not require the identification of a fixed reference point. In general, we can approximate the experimental trajectory as a drifting ellipse-based spiral, with noise:

$$\begin{cases} R(t) = R_A(t) + (r(t) + \tilde{r})\cos(\theta(t) + \tilde{\theta}) \\ Z(t) = Z_A(t) + \zeta(t)\,(r(t) + \tilde{r})\sin(\theta(t) + \tilde{\theta}) \end{cases}$$

$$\begin{cases} r(t) = r_0 e^{\int_{t_0}^{t} \gamma(\tau)d\tau} \\ \theta(t) = \theta_0 + 2\pi \int_{t_0}^{t} f(\tau)d\tau \\ R_A(t) = R_{A,0} + \int_{t_0}^{t} V_R(\tau)d\tau \\ Z_A(t) = Z_{A,0} + \int_{t_0}^{t} V_Z(\tau)d\tau \end{cases}$$

§ From now on we will use indifferently ξ or ξ_{SXR} for the SXR-derived displacement since we have no access to the real core displacement

Where $\left(\tilde{r}, \tilde{\theta}\right)$ are the noise/uncertainty levels respectively on the radius and the poloidal position, $\zeta(t)$ is the ellipticity, $\gamma(t)$ is the growth rate, $f(t)$ is the frequency and A is the center of the spiral, dritfing at speed $\underline{V}_A(t)$. With this definiton, the surface of the 'instantaneous' ellipse, tangential to the trajectory at time t is $S_E = \pi\zeta r^2$, from which we can define the ellipse-based displacement as a generalised geometrical radius $\xi_E = \sqrt{S_E/\pi} = r\sqrt{\zeta}$.

To estimate S_E, we compute the surface spanned during one period of the trajectory, as illustrated in Fig 7 in an ideal case (fixed center, constant growth rate, constant ellicpticity, constant frequency, no noise...). Here, the ellipse E corresponding to chosen point $M(t)$ appears in dashed red line, the fraction of trajectory corresponding to $t \pm T/2$ where $T = 1/f$ is delimited by points $M \pm T/2$ and the correspondig surface $S(t) \approx S_E$ is shaded in grey, the spiral center A is indicated as well as the center of mass B of $S(t)$ which provides a zero-order approximation of A (see Appendix B for more details and error estimates).

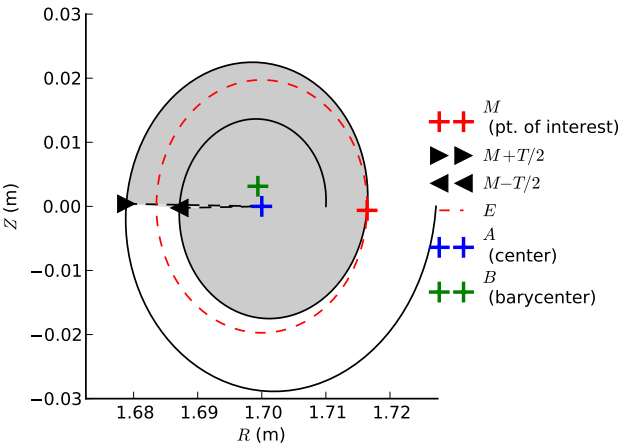

Figure 7: Illustration of the principle used to define a robust displacement from a spiralling trajectory in a surface-based approach.

This surface-based definition $\xi = \sqrt{S/\pi} \approx \sqrt{S_E/\pi} = r\sqrt{\zeta} = \xi_E$ provides a generalised geometrical radius, that gives the same result for a circle and for an ellipse of equal surface, thus reducing the influence of plasma elongation. Moreover, it also smoothes out possible errors on occasional points and, in this respect, has similar effect as a running-average. Furthermore, since the surface spanned during one period is updated for each time step, it follows the drift of the spiral center.

Quantitatively, the surface S_E of the red ellipse is

well approximated by the grey surface S (spanned by the spiral in one period) if the growth rate of the spiral is smaller than its frequency. In this case, the exceeding grey surface (i.e. the fraction that lies outside of the red ellipse) is a good approximation of the missing surface (i.e. the missing part in the red ellipse). The approximation is better with quasi-constant γ, f and ζ. As shown in Appendix A for a circular case ($\zeta = 1$), the approximation scales as:

$$\lim_{\gamma \ll f} \frac{\xi}{r\sqrt{\zeta}} \approx \lim_{\gamma \ll f} \sqrt{\frac{\sinh(\gamma/f)}{\gamma/f}} = 1$$

Of course, real experimental data comes with other difficulties, like changing frequency, elongation or growth rate.

Generally, this definition of the displacement is reliable under the following conditions, where Δ refers to the variation over one mode period:

(i) The frequency changes slowly: $\frac{\Delta f}{f}(t) \ll 1$

(ii) The ellipticity changes slowly: $\frac{\Delta \zeta}{\zeta}(t) \ll 1$

(iii) The growth rate changes slowly: $\frac{\Delta \gamma}{\gamma}(t) \ll 1$

(iv) The growth rate is small $\gamma \ll f$

(v) The drift speed is small: $r(t) \gg \frac{\|v_A\|}{f}(t)$

(vi) The sampling frequency is sufficient $f_S/f > 6-7$

Indeed, quantities like (i) the frequency (known by FT of key signals), (ii) the ellipticity (estimated from background equilibrium) and (iii) the growth rate (checked a posteriori) should change slowly compared to the mode period. This is generally true, except in the very last growth phase when condition (iii) might not be satisfied, thus inducing larger error bars on the displacement. Also, (iv) the growth rate should be small compared to the mode frequency, as was shown be the error derivation. This is also not always true in the last growth phase. However, numerical applications show that the error remains within 10 % with realistic ellipticity, even with $\gamma = 2f$ (cf. Fig. 9). It can go up to 25 % for $\gamma = f$ with very strong ellipticity ($\zeta = 2$, cf. Appendix A). Consequently, we still use this method for the last growth phase as it still gives access to a rough estimate of the displacement.

Additionally, (v) the drift speed of the spiral center should be small compared to the spiral dynamics, this is almost always verified.

Finally, surface S is approximated by a polygon, and the precision of this approximation depends on the sampling frequency f_S (vi). Also, the polygon library used cannot compute the surface of a self-intersecting polygon (as might happen due to noise or limited spatial resolution). To circumvent these two limitations, the "ideal" definition given above is slightly modified by taking instead the convex hull of a fraction $\kappa \in]0.5;1[$ of the polygon representation of S (see Appendix A for details). This fraction is necessarily a multiple of f_S/f. In our case, the high frequency of the SXR diagnostics generally allows to have $\kappa \approx 0.9$ ($f_S/f > 10$). The result is a numerically robust approximation of the surface, which remains close to the surface of the red ellipse S_E.

The accuracy of the method is numerically assessed in Fig 8, which shows the reconstruction of ξ from a phantom case (i.e. analytically known input) representative of a typical AUG experiment. In particular, the mode frequency ($f \approx 20$ kHz), the growth rate ($\gamma \approx 10$ kHz) and the ellipticity ($\zeta \approx 1.4$) are not constant but slowly changing, the center of the spiral is slowly drifting (≈ 141 m/s) and the sampling frequency is 200 kHz. There is also 2 mm random noise on the radial position and $\pi/64$ on θ.

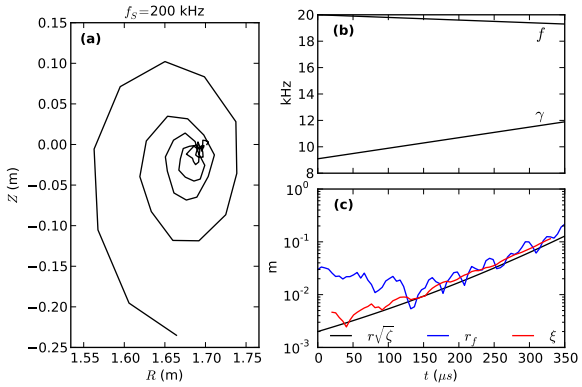

Figure 8: (a) Realistic phantom spiral trajectory, with drift, noise, ellipticity and finite sampling (b) Non-constant mode frequency and growth rates (c) Input radius $r\sqrt{\zeta}$ (black), naive estimate r_f from a fixed point (blue) and proposed surface-based displacement ξ (red).

The proposed displacement ξ (red in (c)) provides good reconstruction of $r\sqrt{\zeta}$ and of its dynamics (i.e.: the growth rate $\gamma = \partial \ln(\xi)/\partial t$) despite non-ideal conditions of use, thus demonstrating its robustness. Also visible (blue) is a naive approach (fixed-point), where the effects of noise, ellipticity and slow drift (responsible for the discrepancy at low displacement) are visible.

Nevertheless, the SXR maximum is not the displaced core. We must then evaluate how well the whole method retrieves the displacement and growth rate of a spiraling core from the SXR maximum using the same tool as in section 2.3.

Simulating such growing modes with this tool implicitly supposes that the W density has time to re-equilibrate while the mode is growing, which translates into $\gamma \ll v_{Th,W}/\pi R_0$ [36], where $v_{Th,W} = \sqrt{8k_B T_W/\pi m_W}$ is the thermal velocity of W (if the mode grows too fast, there is a risk that the SXR maximum may be a W 'bubble' lagging behind the fast displaced core). Hence, the growth rate is constrained both by a technical reason ($\gamma \leq f$) and by a physical one ($\gamma \ll v_{Th,W}/\pi R_0$). It is thus a general limitation of the presented work. Fortunatelly, as previously stated, this condition is experimentaly often fulfilled, except in the last phases which sometimes display $\gamma \approx f$ and $\gamma \geq v_{Th,W}/\pi R_0$, which is the limit of the proposed method in its current state.

In Fig 9, several growing modes are displayed, with $f = 15$ kHz and γ ranging from 1 to 30 kHz. In each case, ξ_{SXR} is compared to the input core displacement to assess how constraining the technical limitation is.

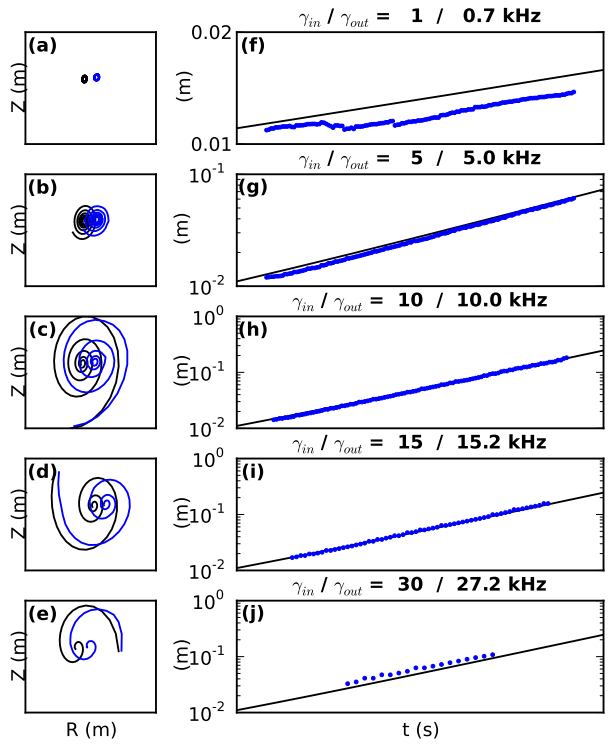

Figure 9: (a-e) Trajectories of the displaced core (black) and shifted SXR maximum (blue) for $f = 15$ KHz and $\gamma \in$ [1,5,10,15,30] kHz with the same scale (f-j) Corresponding input core displacement (black) and ξ_{SXR} (blue points). Titles show the input and SXR-retrieved γ values. Discrepancies at low displacement for $\gamma = 1$ kHz are numerical errors ($\approx$ mesh size).

In all cases the growth rate is retrieved with very good precision (cf. titles) and, remarquably enough, even for cases which are in principle out the domain of validity of our method, with $\gamma = f$ and $\gamma = 2f$. Hence, the technical limitation is not so restricting, but the physical one remains (i.e. W transport, not accounted for in this code).

Finally, Fig 10 shows, from AUG experimental cases, that ξ is hardly affected by the regularisation, thus concluding the demonstration initiated in 2.2 with the same two cases. Interpretation of the behaviour of these two particular cases will be addressed in a later paper, here they simply illustrate the technical robustness of the proposed method.

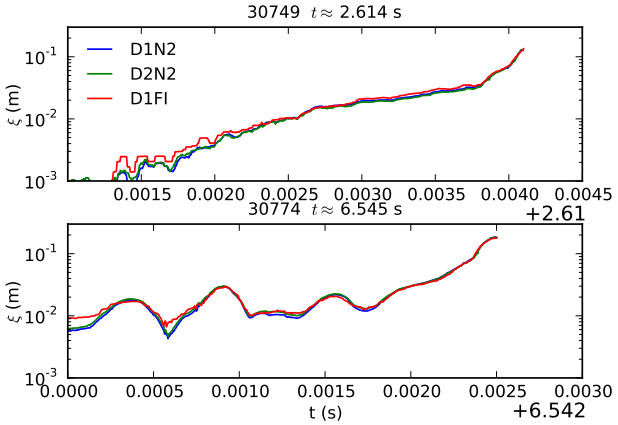

Figure 10: Displacement ξ for the same 2 AUG crashes and 3 regularisations described in 2.2.

In summary, we know that for *peaked* SXR profiles:

(i) The SXR diagnostic and tomography give access to a robust reconstruction of the trajectory of the SXR maximum

(ii) This trajectory is a reliable proxy of the trajectory of the displaced core

(iii) The displacement and growth rate of the core can be retrieved via this proxy, thanks to a numerically robust definition of the displacement

(iv) There is a weak technical limit ($\gamma \leq f$), but a possibly stronger physical limit ($\gamma \ll v_{Th,W}/\pi R_0$) to the method validity.

We can now use this method to study experimental cases. However, before going further, it should be underlined that the terminology used to characterize sawtooth crashes is not always practical when it comes to defining quantities from experimental data. Hence, the next section proposes a number of quantitative definitions based on the data that is accessible via the proposed method.

3. Defining the crash reference time, crash duration, growth phases and other quantities

The proposed method is only valid for peaked SXR profiles, so it is usually *not* usable to characterise the displacement of a postcursor as the post-crash profile is usually flat or hollow. Nonetheless, all studied cases clearly display a postcursor mode that closely resembles a continuation of the precursor (same frequency and location, in particular we observe no shift of the mode poloidal position), which suggests incomplete reconnection.

This remark underlines the necessity to define exactly what is meant by "precursor", "crash" and "postcursor". Indeed, as already stated in [52], the vocabulary used by the tokamak community is sometimes a bit sketchy and lacks accurate quantitative definitions that could be used experimentally. In particular, the distinction between pre- and post-cursor oscillations is a bit artificial since a so-called precursor oscillation may survive through the crash with identical frequency, localisation and similar amplitude.

In the framework of this article, we propose to define a reference time for each sawtooth crash and to call *precursor* all contiguous - from the point of view of frequency and displacement - 1/1 mode activity that precedes this reference time, and *postcursor* all contiguous 1/1 mode activity that follows it. More specifically, we propose two definitions for the reference time:

(i) t^{ξ}_{Ref} is the first time at which the displacement reaches its absolute maximum.

(ii) t^{ϵ}_{Ref} is the time at which the the value of the SXR emissivity maximum has the largest derivative.

These two definitions typically agree within a few tens of microseconds (giving an indication of how well the crash instant is identified), and they are complementary because while t^{ξ}_{Ref} is derived from a spatial information, t^{ϵ}_{Ref} is derived from a SXR intensity information, two different aspects of tomographic inversions. Despite the fact that the absolute value of the SXR emissivity maximum (ii) is *not* a robust quantity with respect to tomography method, its relative time evolution is more so, as illustrated in Fig 11, which justifies its use to define t^{ϵ}_{Ref}.

While t^{ξ}_{Ref} is the time of maximum displacement, t^{ϵ}_{Ref} is the time when the effect of the reconnection on the SXR emissivity is the most visible. When the SXR profile stops being peaked (usually shortly after t^{ξ}_{Ref}), the value of ξ computed by our method stops being relevant.

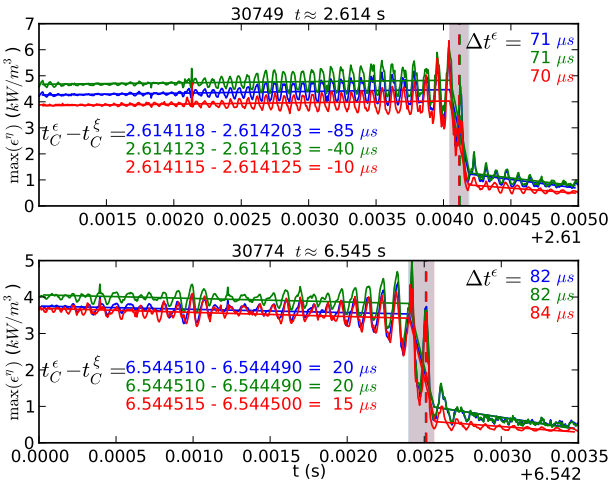

Figure 11: Time traces of the absolute value of SXR maximum for 2 crashes (with same 3 regularisations as in Fig. 3). The relative time evolution is robust and can be used to define a reference time t^{ϵ}_C and a crash duration Δt^{ϵ} from the best fit of 3 lines.

As far as the crash duration is concerned (we voluntarily avoid the term "crash time" to avoid confusion between a reference instant and a duration), we propose two experimental definitions:

(i) Δt^{ϵ} is the time it takes for the SXR maximum emissivity to drop.

(ii) Δt^{ξ} is the duration of the main growth phase of the precursor.

Indeed, Δt^{ϵ} can be derived from the relative time evolution of the SXR emissivity maximum. The best possible fit is found for a 3-piece linear function and the time interval corresponding to the middle linear function is Δt^{ϵ}, as illustrated in Fig 11.

It is more difficult to derive a robust definition Δt^{ξ} from the displacement. Indeed, the precursor growth is typically a multi-phase process where each phase seems to have its own dynamics. Empirically, the displacement can usually be approximated, in logarithmic scale, as a series of piece-wise linear growth phases. Here the term *linear* clearly refers to the empirical shape of the plot and does not necessarily imply linearisation of the MHD equations. Although there are some exceptions to this observation, we decide, as a first step, to systematically decompose the logarithm of the displacement as a set of piece-wise linear functions, the slope of which is then used to define the growth rate γ_i (for phase i). The quality of the fit is estimated by the 95 % confidence bounds from which error bars on the growth rate can be derived. Each phase can also be characterised by the time Δt_i and displacement $\Delta \xi_i$ it spans. If the phase duration Δt_i

is to be compared to any reference "crash time" from literature, it should be corrected by a factor $\xi_{max}/\Delta\xi_i$ to take into account the fact it does not correspond to full reconnection but only to a fraction of it (see Appendix C for detailed derivations). Hence, this correction will be done for each growth phase, and the displacement-based crash duration is defined as the corrected duration of the phase that represents the largest reconnected fraction $\Delta t^{\xi} = \Delta t_I \times \xi_{max}/\Delta\xi_I$ where $\Delta\xi_I/\xi_{max} = \max_i(\Delta\xi_i/\xi_{max})$. While this definition is sufficient for the 3 cases presented in this paper, attention of the community is drawn to the fact that it is not always so.

As far as comparison with linear theory is concerned, the growth rate γ_i of each phase will be compared to the 1/1 resistive kink linear growth rate γ_R, and its corrected duration $\Delta t_i \times \xi_{max}/\Delta\xi_i$ to Kadomtsev-based "crash times". All the following literature-derived quantities are estimated from plasma parameters in the vicinity of the q=1 surface, itself estimated from the maximum displacement ξ_{max} and remapping on the background equilibrium:

- The poloidal Alfven time, computed from the poloidal field at q=1: $\tau_{A,\theta} = \frac{\xi_{max}}{B_\theta/\sqrt{\rho\mu_0}}$
- The reconnected flux Alfven time, estimated from $B^*_\theta \approx (1-q_0)B_\theta$, with $q_0 = 0.9$ for all cases because it is not well-measured [53]: $\tau^*_A = \frac{\xi_{max}}{B^*_\theta/\sqrt{\rho\mu_0}}$
- The resistive diffusion time, estimated from the Spitzer resistivity η [54]: $\tau_{RD} = \frac{\mu_0\xi^2_{max}}{\eta}$
- The Kadomtsev reconnection time (with resistivity only in Ohm's law) [10]: $\tau_{K,\eta} = \sqrt{\tau_{RD}\tau^*_A}$
- A modified Kadomtsev reconnection time (with electron inertia only) [8], using the plasma angular frequency $\omega_P = \sqrt{\frac{n_e e^2}{\epsilon_0 m_e}}$: $\tau_{K,e} = \xi_{max}\frac{\omega_P}{c}\tau^*_A$
- A modified Kadomtsev reconnection time (with electron viscosity only) [11], using the electron thermal velocity $v_{Te} = \sqrt{\frac{k_B T_e}{m_e}}$ and acceleration length $L \approx \xi_{max}\frac{B}{B^*_\theta}$: $\tau_{K,v} = \xi_{max}\frac{\omega_P}{c}\sqrt{\frac{\tau^*_A L}{v_{Te}}}$
- The 1/1 resistive kink growth rate from [54] (p.333): $\gamma_R = \frac{1}{\left(\tau^{*2}_A\tau_{RD}\right)^{1/3}}$

In addition, and since all the considered SXR profiles are peaked, it is possible to quantify the peaking of the 2D reconstructions by defining a *peaking factor* $\Pi = S_P/S_{FWMH}$, where S_P is the total plasma surface and S_{FWMH} is the surface of the iso-contour at mid-height. Care must be taken as the absolute value of Π *does* depend on the regularisation used. Hence, comparisons are only relevant for identical regularisations, or if only its relative time evolution is considered.

The position of the $q = 1$ surface can be estimated from the maximum displacement ξ_{max} in two ways. On the one hand, an extrapolation of the trajectory ellipticity allows to plot the "maximum ellipse" corresponding to the maximum displacement (this ellipse can then be remapped on the background equilibrium to average out possible errors). On the other hand, the background equilibrium can be used to determine which flux surface has an area matching ξ_{max}. Both approaches give similar results, and when necessary the remapping is done on the toroidal flux coordinate ρ_T because unlike ρ_P it does not depend on the uncertain current profile.

Finally, as far as the quantification of the 1/1 mode frequency is concerned, a usual method consists in performing the FT of a single central SXR channel. While this method is pretty straighforward, it may miss the existence of the mode in its early growth phase if its trajectory lies entirely inside the VOS of the selected channel. Furthermore, extra harmonics may be found in the spectrum, due to very peaked radiation profile or when the VOS only intersects a fraction of the trajectory. Such extra harmonics are misleading as they do not necessarily correspond to *physical* mode harmonics. Finally, if higher mode harmonics are really physically present in the plasma (like 2/2 or 3/3), their influence will also be visible on the spectrogram of the selected channel. Hence, in order to accurately focus on the quantification of the 1/1 mode frequency only, even for small displacements and at the exclusion of other modes influence, we choose to perform the spectrogram of the Z-coordinate of the SXR maximum trajectory. Indeed, while a single channel may miss part of the dynamics, SXR inversions provide a result that takes into account all channels. And we saw that for peaked profiles the position of the SXR maximum is well-constrained such that even small movements are reconstructed. Moreover, higher harmonics like 2/2 or 3/3 modes should in principle not affect the core displacement significantly and their influence on the spectrogram is thus naturally eliminated. Furthermore, the Z coordinate is chosen over the R coordinate to get rid of the possible influence of the LFS-HFS asymmetry induced by the presence of W in a rotating plasma. Finally, since the objective is to track the main frequency of the 1/1 mode, all spectrograms are normalised to their maximum value at each time step. We empirically find that this method provides very clean spectrograms as far as the 1/1 mode frequency is concerned, for *peaked* SXR profiles.

In the following, the proposed method is applied to three examples representative of the diversity of sawtooth crashes in ASDEX Upgrade.

4. Evidence of non-monotonic growth rates for typical AUG crash precursors

The 3 chosen cases yield interesting quantitative observations regarding the time evolution of the growth rate. They are extracted from a larger database of ≈ 100 AUG crashes that will be explored in a further publication. Since it was shown that the inversion method had virtually no effect on the quantities of interest, and for readability purposes, we show results computed with one regularisation only (D2N2). Some key plasma parameters, measured before the crash, can be found for each case in table 2. For easier comparison, the characteristics of a non-linear bi-fluid MHD simulation in cylindrical geometry presented in section 4.2 are also included here.

Table 2: Shot characteristics
q_0 is assumed to be 0.9 in experimental cases
ξ_{max} and r_{inv} are remapped to ρ_T for information

Name	Case 1	Case 2	Case 3	Simu.
shot	31579	30532	30774	-
t (s)	2.842	2.554	6.694	-
Gas	D	D	D	D
I_P (MA)	0.8	0.8	0.8	0.53
B_T (T)	-1.8	-2.4	-2.5	2.0
P_{NBI} (MW)	4.7	1.7	4.8	-
P_{ECRH} (MW)	1.7	0	0	-
P_{ICRH} (MW)	0	0	0	-
$T_e(0)$ (keV)	2.7	2.7	2.3	2.0
$n_e(0)$ $(10^{19}\ /m^3)$	6.8	3.5	10.3	3.0
$v_{rot}(0)$ (km/s)	95	120	100	0
q_0	(0.9)	(0.9)	(0.9)	0.91
q_{95}	-3.94	-4.69	-4.69	2.75 (cyl.)
Z_{eff}	3.3	4.5	2.6	1.
β_N	1.65	0.52	1.54	-
Peaking Π	40-50	40-50	80-90	-
ξ_{max} (cm)	20	18	14	18
r_{inv} (cm)	22	20	14	-
$r(q=1)$ (cm)	-	-	-	15
ξ_{max} (ρ_T)	0.31	0.27	0.23	-
r_{inv} (ρ_T)	0.34	0.30	0.23	-
Δt^{ϵ} (μs)	108	79	652	-
Δt^{ξ} (μs)	445	264	556	85
$\Delta t^{\epsilon}/\tau_{A,\theta}$	326	455	1875	-
$\Delta t^{\xi}/\tau_{A,\theta}$	1350	1556	1590	283
τ_{RD} (s)	1.6	0.65	1.0	2.1
$\tau_{A,\theta}$ (μs)	0.33	0.17	0.35	0.30
$\tau^*_{A,\theta}$ (μs)	3.3	1.7	3.5	3.3
$\tau_{K,\eta}$ (ms)	2.3	1.1	1.9	3.0
$\tau_{K,e}$ (ms)	0.96	0.28	0.87	0.12
$\tau_{K,v}$ (ms)	0.49	0.22	0.48	0.25
γ_R (kHz)	3.9	8.0	4.3	3.1
$\omega^*_e/2\pi$ (kHz)	2.3	5.4	-	6.9
$v_{Th,W}/\pi R_0$ (kHz)	11.6	11.6	10.7	-
Precursor type	Fish. -like	Multi -harm.	Slow	

In the following, robust observations on the displacement and growth rate are drawn from the proposed method in each case, and possible interpretations for the specifity of each crash are then discussed. To highlight the tendencies and uncertainties, the growth rates will not only be estimated in a piece-wise manner, but also fitted by b-splines. Finally, it should be kept in mind that quantities introduced for comparison with literature, like $\tau_{K,\eta}$, $\tau_{K,e}$, $\tau_{K,v}$ or γ_R, are only orders of magnitude since they depend on $1 - q_0 \approx 0.1$ for all cases (uncertainty $\approx$ one order of magnitude).

4.1. Displacement and growth rate

Case 1 is a typical precursor happening during a fishbone instability, common on AUG. Indeed, in NBI-heated plasmas, trapped fast ions may transiently destabilize 1/1 modes. This so-called "fishbone" instability [55] is visible as a transient 1/1 mode on SXR channels. Its lifetime is typically a few milliseconds and it is characterized by a drop in 1/1 frequency due to the redistribution of fast ions (i.e. the drive) in velocity and/or physical space as the mode grows [56]. We observe many crashes preceded by fishbones, and sometimes the precursor itself is initiated in a fishbone-like manner.

The experimental recipe to identify fishbones is to spot 'inverted comma' shapes in the spectrogram of a central SXR channel. Here it is done with the spectrogram of the Z-coordinate (cf. 3). Signs of 1/1 activity are also visible on the SXR maximum and on the behaviour of ξ, as seen in Fig 12.

The four fishbones are clearly identified, as well as the precursor which starts like a fishbone from the point of view of the frequency, displacement and growth rate. A reproducible pattern appears. A closer look at the displacement and growth rates during the fishbones and precursor can be obtained by overlaying them all over one another, as illustrated in Fig 13.

The precursor growth rate clearly decreases before suddenly surging, suggesting a sudden change in the growth regime. The fact that the growth rate is numerically close to the linear growth rate of a resistive kink mode does not necessarily mean that the growth is linear, indeed, both the non-monotonicity and the sudden changes support the idea of non-linear growth through the whole phase. The global picture seems rather to be that of a non-monotonic non-linear growth rate that simply happens to be numerically close to a linear growth rate.

Regarding the onset criterion and the reason why this particular fishbone leads to a crash, no conclusive observation could be made with available data. This aspect remains to be investigated.

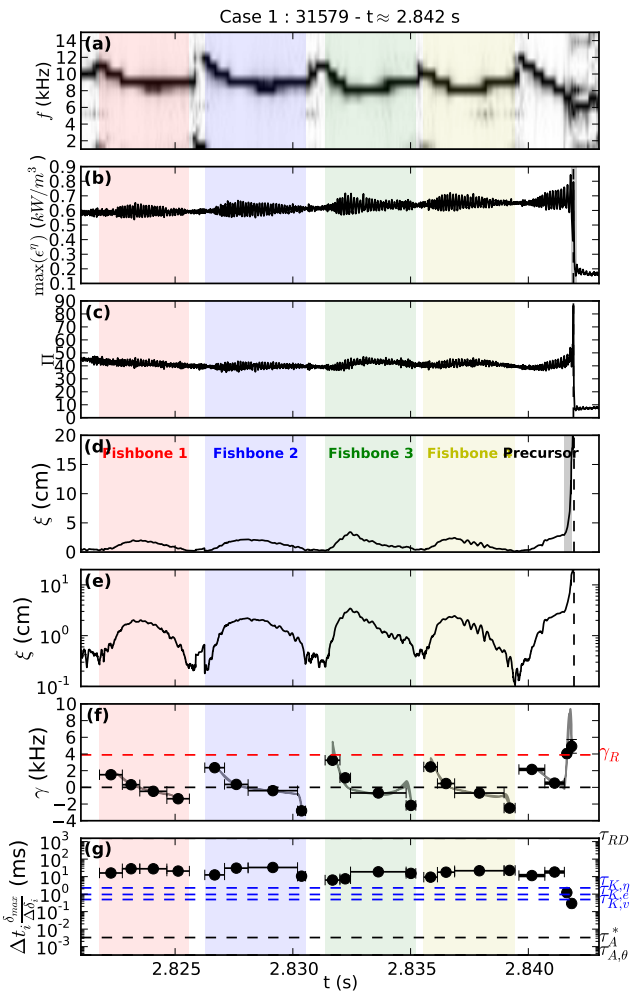

Figure 12: (a) Spectrogram (b) SXR maximum value with Δt^{ϵ} (grey shaded area) (c) peaking factor (d) displacement in linear scale with non-corrected Δt^{ξ} (grey shaded area) and (e) in log scale (f) growth rates and (g) phase durations of a precursor preceded by 4 fishbones on ASDEX Upgrade.

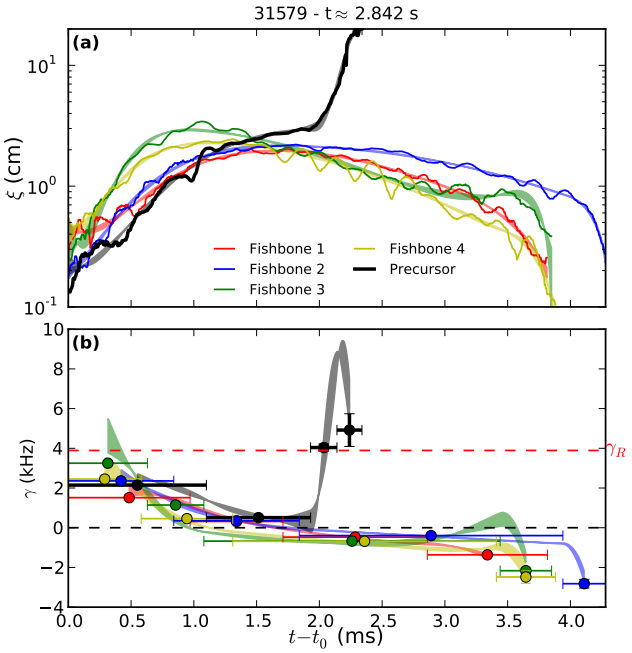

Figure 13: Superimposition of fishbones and precursor phases, with the same color code as in Fig 12, to compare the (a) diplacement in log scale and (b) growth rates.

Case 2 is also quite common in AUG. It is a case for which the non-monotonicity is also clear but with no visible fishbone activity before or during the precursor. In fact the mode frequency is almost constant (slightly increasing) through the whole phase. In Fig 14, the mode growth is clearly damped during phase 2.

The growth rate decreases between phases 1 and 2, before increasing again in phase 3. It is almost constant in all three phases. This hightlights both the piece-wise behaviour and the non-monotonicity. Then, a sudden regime change takes place and the growth rate surges in phase 4, up to values comparable to the mode frequency. As was shown in Fig 9 and Appendix A, the proposed method should be technically valid (≈ 10 % error in such cases). However the physical limit may be reached here and W transport may be somewhat slower than the reconnection during a short time at the beginning of phase 4, as the measured growth rate transiently exceeds $v_{Th,W}/\pi R_0$, this aspect is the main unknown. Notice again how the growth rate is of the same order of magnitude as γ_R, while its behaviour clearly indicates non-linearity.

This case illustrates the difficulty of defining the "precursor". One could argue that it is the collection of phases 1-3 and that phase 4 should be called the "crash", based on the clear slope break of the displacement between phases 3 and 4. But the behaviour of both ξ and f suggest that this is all the same mode that simply crosses a threshold at some point. Hence, we choose to call "precursor" the whole sequence (phases 1-4). Also, the slope break is not always so visible and there are sometimes several slope breaks, and the fastest growth phase is not always the very last one, as we will see in Case 3, such that a decision based only on this criterion would hardly be applicable to all cases.

Case 3 is a less common, but not rare, slow crash. This behaviour, illustrated in Fig 15, recalls the crash "of the 2nd kind" presented in [52] on Tore Supra. In particular, the time evolution of the displacement is similar, with a fast and then steady increase.

This case is representative of the difficulty of defin-

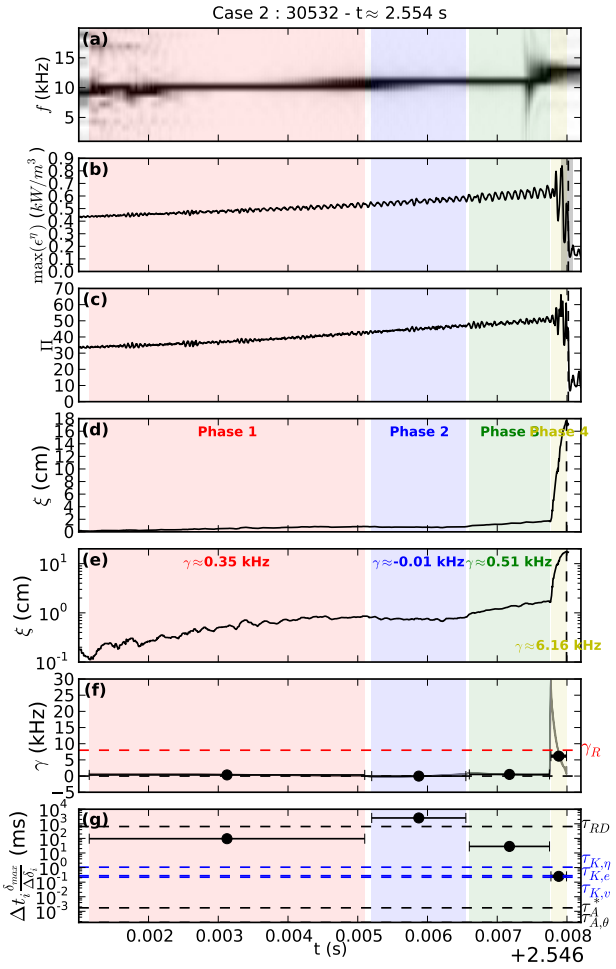

Figure 14: (a) Spectrogram (b) SXR maximum value with Δt^{ϵ} (grey shaded area) (c) peaking factor (d) displacement in linear and (e) log scale (f) growth rates and (g) phase durations of a precursor without fishbone on AUG. Here Δt^{ξ} is computed from phase 4.

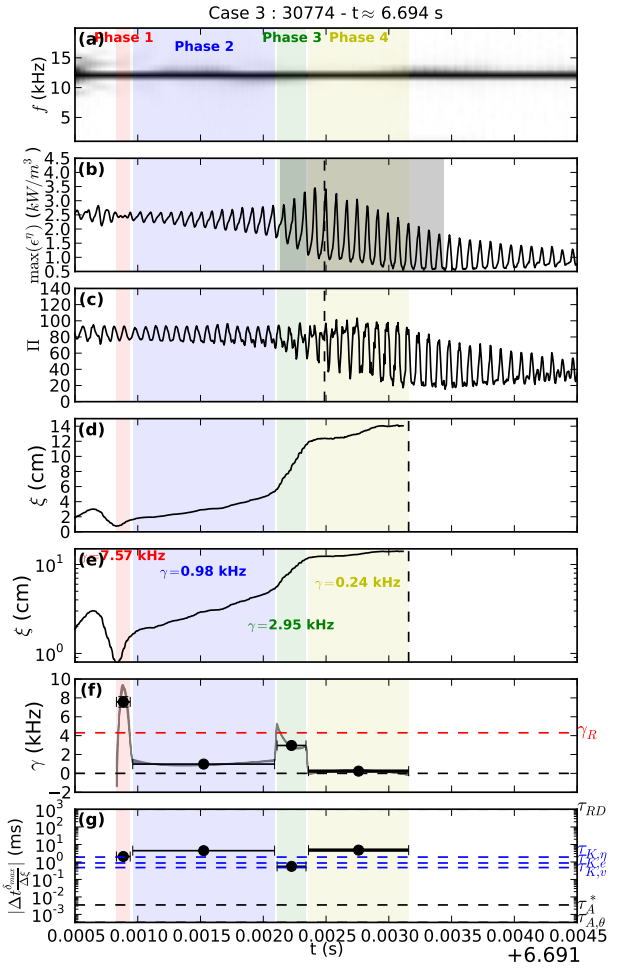

Figure 15: (a) Spectrogram (b) SXR maximum value with Δt^{ϵ} (grey shaded area) (c) peaking factor (d) displacement in linear and (e) log scale (f) growth rates and (g) phase durations of a slow precursor on AUG. Here Δt^{ξ} is computed from phase 3. The vertical dahsed lines are t^{ϵ}_{Ref} (first) and t^{ξ}_{Ref} (second).

ing the reference time. Here t^{ξ}_{Ref} and t^{ϵ}_{Ref} do not match as well as for fast crashes, and there is almost 1 ms of discrepancy. Similarily, it illustrates how the terms "precursor" and "postcursor" may sometimes seem superficial. Indeed, given the unchanged frequency and the clear continuation of the mode activity throughout the crash, one could argue that there is no reason to consider two distinct phases. Nevertheless, we follow the criteria introduced in section 2 (i.e. no clear discontinuity in frequency and displacement) and consider phase 4 to be part of the precursor and t^{ξ}_{Ref} to be the good reference time. This choice, however questionable, is supported by the fact the SXR profile stops being clearly peak after t^{ξ}_{Ref}, which also means the displacement computed after it cannot be considered relevant and is thus not shown.

Again, it is clear that the sawtooth precursor growth rate does not undergo a monotonic increase and that it often displays a piece-wise quasi-constant behaviour suggesting sudden regime changes. Also, the fastest growth phase is not the last but the first one.

The slowness of the crash is tentatively quantitifed in table 2 by its Δt^{ϵ} and Δt^{ξ}, absolute or normalised by the poloidal Alfven time scale $\tau_{A,\theta}$, with the values obtained in the two previous cases. All estimates show a longer crash.

4.2. Interpretation

In this sub-section we use and illustrate another capability permitted by the presented method: the fine tracking of the mode frequency together with its dis-

placement and its remapping to the bulk plasma rotation profile for comparison. We also investigate the importance of higher harmonics for Case 2 and of the pressure gradient for Case 3.

Case 1 The relationship between the fast ions and the precursor is not completely clear. It has been reported in literature [57, 58] that when sawtooth crashes happen during fishbones, the crash often occurs in the phase of maximal fishbone amplitude. This is also observed here, as clearly visible in Fig 13. It suggests a strong iteraction between both instabilities, like mode coupling or stabilisation of the 1/1 precursor by fast ions until they are redistributed [58, 59]. This supports the idea that the fishbone should be considered as part of the precursor itself.

In Fig 12 (a), the mode frequency does not stabilize at the same low value as for the preceding fishbones ($\approx$ 9 kHz), instead it keeps on decreasing to a lower value ($\approx$ 6 kHz). We can propose an interpretation in the light of Fig 16, which displays the mode frequency, its displacement, and the plasma toroidal rotation profiles before and after the crash, as measured by the charge exchange diagnostics. Two phases (A) and (B) are indicated, and the points delimiting them are remapped (from frequency (a) and displacement (b) via background equilibrium reconstruction) to a toroidal rotation velocity (c) for comparison with the rotation velocity profile measured by charge exchange.

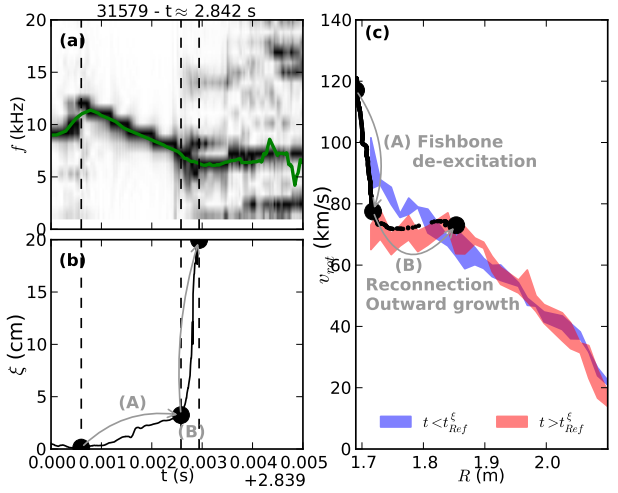

Figure 16: (a) Spectrogram with smooth main frequency (green solid line) and (b) displacement of a precursor (same as in Fig 12) (c) Plasma toroidal rotation profiles before (peaked) and after (flattened) the crash from charge exchange, with remapped mode frequency (black dots).

During a normal fishbone, the mode frequency is aligned on the fastest trapped ions frequency. Then, due to removing of the drive (i.e. of the most energetic fast ions), the frequency decreases. For the precursor, this happens during the first phase (A), and then the remapping of the mode frequency and displacement on the bulk rotation profile in phase (B) suggests that reconnection has started, thus forcing the mode frequency to align to the bulk plasma rotation at $q = 1$ for the fast growth phase.

The estimated electron diamagnetic frequency ω_e^* (cf. table 2) should translate into $\approx$ 22 km/s if remapped to rotation velocity. Remarquably, there does not seem to be any noticeable influence of ω_e^* on the resistive mode frequency which almost perfectly matches the bulk plasma rotation at $q = 1$ in phase (B). However, the value in table 2 corresponds to phase (A), and its evolution in phase (B) could not be checked due to noise and missing data.

Case 2 As opposed to Case 1, here the mode frequency slowly increases up to the crash reference time. A look at the measured plasma rotation velocity and its time evolution provides 3 possible and complementary interpretations. First, as seen in Fig 17 (c), the whole rotation profile undergoes a steady increase throughout the whole sequence (i.e. the profile after the crash is the same as before the crash, within error bars, but translated to higher values). Hence, at any fixed position, the mode frequency would increase with time if the mode is resistive. Second, the error bars are compatible with a slightly hollow rotation profile, itself compatible with the 2 tangential NBI sources used for this shot with an off-axis deposition layer ($\rho_P \approx 0.1-0.2$ according to the background equilibrum reconstruction). In the case of an initially ideal mode with low frequency, its frequency would increase as it turns into a resistive mode and reconnects on the $q = 1$ surface. Third, the role of the electron diamagnetic frequency (estimated from the global pressure gradient inside $q = 1$) is unclear, but we observe that it decreases during phase (B). Since ω_e^* and the bulk plasma rotation go in opposite directions, a decrease of the former *could* translate into an increase of the resistive mode frequency observed in the laboratory frame (that is, if ω_e^* has any influence on the mode frequency, which may become true as the mode changes regime but is difficult to check).

This analysis of the mode frequency does not provide any explanation for the transient growth rate damping observed during phase 2 of Fig 14, and there is no visible fishbone activity either. One possible

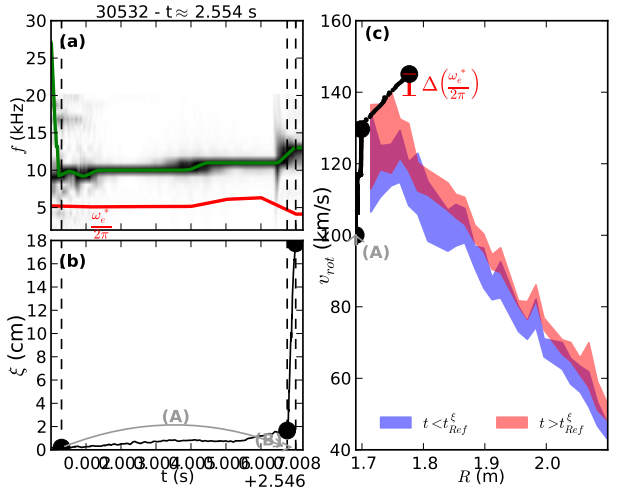

Figure 17: (a) Spectrogram with the electron diamagnetic frequency $\omega_e^*/2\pi$ (red solid line) and (b) displacement of the Case 2 precursor (c) Plasma toroidal rotation profiles before (peaked) and after (flattened) the crash from charge exchange, with the change in rotation associated to the difference in diamagnetic frequency $\Delta\left(\frac{\omega_e^*}{2\pi}\right)$ of phase (B).

explanation lies in non-linear coupling between the first and higher mode harmonics. Indeed, the simulation of a sawtooth crash precursor with of a non-linear bi-fluid MHD code in cylindrical geometry with circular cross-section [60] does show a correlation between a relative increase of the 2nd/1st harmonic energy ratio and a transient growth damping of the 1/1 precursor mode, as shown in Fig 18.

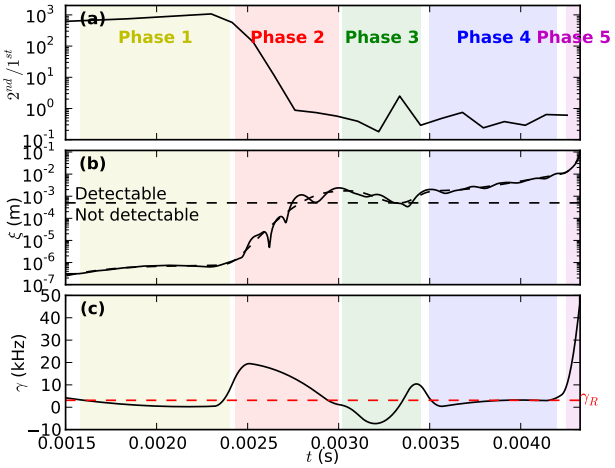

Figure 18: Simulation of a sawtooth crash precurosor using a fully non-linear bi-fluid MHD code in cylindrical geometry. (a) Time trace of the ratio of the maximum of the 2/2 perturbation profile over the 1/1 profile (b) Time trace of the displacement (c) Estimated growth rate.

In addition to the characteristics displayed in table 2, the simulation assumes a perpendicular heat diffusivity of $\chi_\perp = 0.2\ m^2/s$ and perpendicular particle diffusivity $D_\perp = 0.2\chi_\perp = 0.04\ m^2/s$. Finally, the code does not include fast ions (consistently with the absence of fishbone activity in this case).

Among of the main differences of this simulation with Case 2 are the low Z_{eff} value which affects the $\tau_{RD}/\tau_{A,\theta}$ ratio, the cylindrical geometry and absence of toroidal coupling, and the fact that we do not have access to accurate measurements of q_0 in the experiments (0.9 is simply a guess). Despite these differences, the simulation clearly shows a non-monotonic growth rate and, to some extent, a piece-wise behaviour (despite fluctuations). These two key features echo our robust experimental observations. Also, we observe that γ is numerically close to γ_R, like in the experiments.

The whole sequence in Fig 18 can be interpretated as follows: the simulation is started in a situation where the 1/1 mode is stable but the 2/2 mode is just above its linear stability threshold. As this 2nd harmonic grows (phase 1), it locally flattens the temperature profile and destabilizes the 1/1 mode which then becomes dominant (phase 2, the displacement increases as the ratio 2nd/1st decreases). Then, the 1/1 mode is again transiently stabilized by its competition with the 2/2 mode (phase 3, a transient decrease of the displacement corresponds to a transient increase of the 2nd/1st ratio). Finally, the 1/1 mode becomes dominant (phase 4) and leads to a crash (phase 5).

In the light of this simulation, the possibility that the 1/1 mode of Case 2 be transiently stabilized by a competition with a 2/2 mode during phase 2 is now investigated.

The presence of a 2nd harmonic at $\approx$ 20 kHz is quickly confirmed from the spectrograms of central SXR channels. However, this second harmonic could simply be due to the measurement technique and not necessarily to a real 2/2 magnetic perturbation, as explained in section 3 and illustrated in [21] in the case of ECE measurements. This possibility is eliminated thanks to Fig 19 which shows:

- A 2D reconstruction of this 2nd harmonic, with a rotating spatial structure compatible with a 2/2 mode (a)
- The spectrogram of the reconstructed SXR emissivity at point A showing the same 2nd harmonic (b).
- The spectrogram of a ballooning coil, confirming that this - weak but visible - 2nd harmonic corresponds to a magnetic perturbation (c).

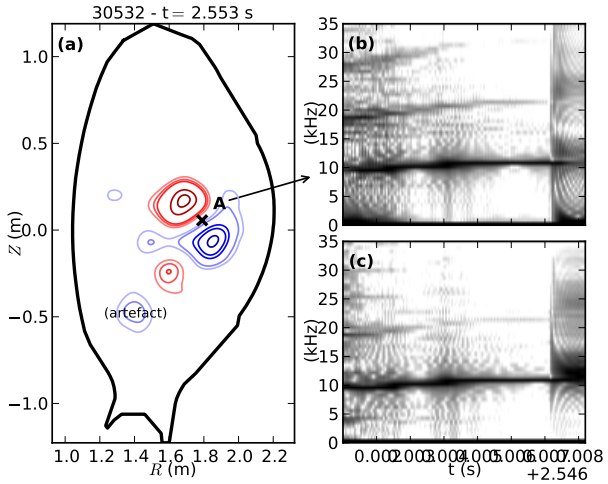

Figure 19: (a) 2D reconstruction of the 2nd harmonic, stronger on the LFS due to W asymmetry (b) Spectrogram of the total SXR emissivity at point A (c) Spectrogram of ballooning coil B31-02. The 2/2 mode is at ≈ 20 kHz

The presence of a real 2/2 mode is thus confirmed. The time evolution of its relative importance over the 1/1 mode can be estimated from the spectrograms. In Fig 20 (b) the 2nd/1st harmonic ratio is plotted. It is computed from the spectrograms of the central SXR channel, of point A and of the ballooning coil, in order to assess the robustness of the observation with respect to the chosen signal.

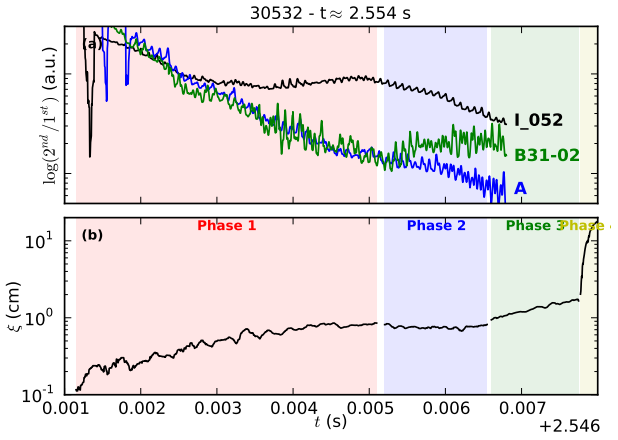

Figure 20: (a) Ratio of the 2nd over the 1st mode harmonic computed from the spectrograms of SXR channel $I_0 52$, of point A and of a ballooning coil, the ratios are normalized to match at $t \approx 0.0025$ (b) Displacement in log scale.

A transient increase of the 2/2 relative importance is observed on the ratio computed from the central SXR channel and from the ballooning coil. Particular care must be taken when interpreting this data, and the following should be kept in mind:

(i) The ratio computed from the SXR channel may be affected by changes in the shape of the signal (peaking, trajectory truncation...).

(ii) The ratio from point A may be smoothed by the inversion since this 2/2 mode is a subtle and weak feature of the reconstructed profile.

In the light of these remarks, we propose the following interpretation: the regularisation smoothes out the transient increase of the 2nd/1st harmonic ratio, explaining why it is not visible on A. The SXR channel includes the physical increase of the 2/2 mode, but also other non-physical contributions, like slowly increased peaking (cf. Fig 14), explaining why the correlation with phase 2 is not as clear as for the ballooning coil.

In summary, a 2/2 mode coexists with the 1/1 mode in the experiment, and there is a transient damping of the 1/1 mode which, as suggested by the simulation, is correlated to an increase of the relative importance of the 2/2 mode. This suggests competition between the two modes, which also supports our general observations (non-monotonicity and more generally non-linearity).

Case 3 The very stable mode frequency observed in case 3 is consistent with a combination of flat central plasma rotation profile and small $q = 1$ surface (i.e. small ξ_{max}), as illustrated in Fig 21.

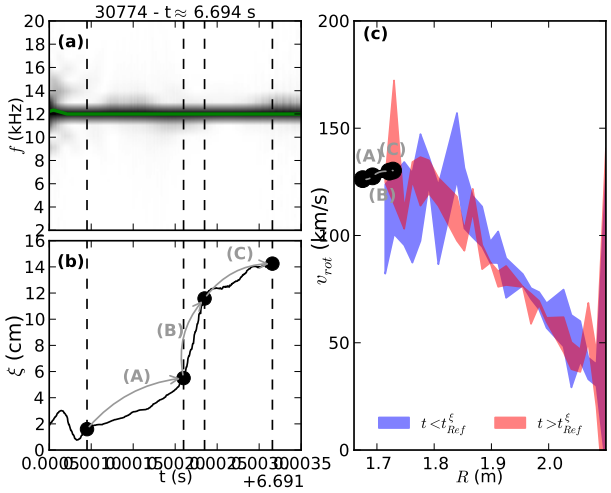

Figure 21: (a) Spectrogram and (b) displacement of the Case 3 precursor (c) Plasma toroidal rotation profiles before and after the crash from charge exchange.

More delicate is the explanation of the slowness of the crash. It was found in recent simulations that crashes with resistive precursors were significantly slower when q_0 is closer to unity [60]. Experimentally accessing an accurate estimate of q_0 is presently impossible on ASDEX Upgrade, but notice that a higher

q_0 (i.e. closer to unity) should translate into a smaller $q = 1$ surface provided the q profile is both monotonic and not too flat in the center. It is not sufficient to conclude beyond reasonable doubt, but it is encouraging and we will try to assess the robustness of this observation with a larger database in a later publication.

As far as linear theory is concerned, the drive of the 1/1 mode in its early phase should be found in the pressure gradient at the $q = 1$ surface. While we know that most of the precursor lifetime corresponds to non-linear growth with large perturbations, it remains interesting to check how the crash duration scales versus a naive extrapolation of the linear theory (i.e.: versus the pressure gradient at $q = 1$ in the early precursor lifetime). This is done in Fig 22 for the two definitions of the crash duration Δt^ϵ and Δt^ξ that we proposed in section 3.

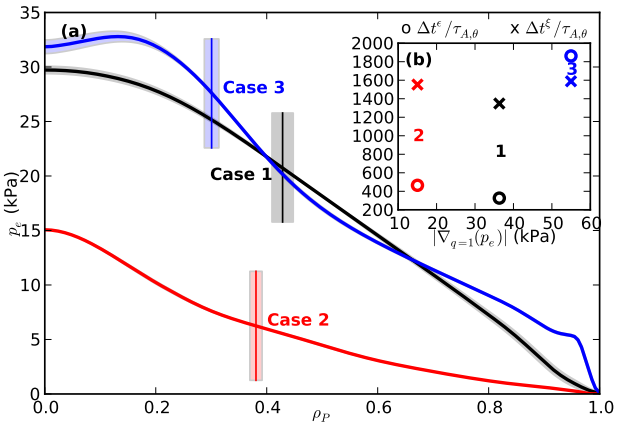

Figure 22: (a) Pre-crash electron pressure profiles for all 3 cases, with the estimated $q = 1$ surface indicated by vertical lines (b) Estimated crash durations Δt^ϵ and Δt^ξ (cf. section 3) versus the absolute pressure gradient at $q \approx 1$.

Contrary to what could be expected from an extrapolation of linear stability theory, both measures of the crash duration show that a larger pressure gradient at $q = 1$ does not cause a faster crash. In fact the correlation even seems to be reversed, particularly for Δt^ϵ. This is yet another confirmation that non-linearity plays a crucial role in the precursor development and crash duration and underlines the relevance of the presented experimental method, the results of which should be compared to non-linear MHD simulations.

5. Conclusions and perspectives

This paper aims at laying the basis of a long-term effort to provide experimental input for validation of sawtooth crash numerical models. In this respect, we proposed a robust, accurate and thoroughly benchmarked method to derive an estimate of the core displacement for crashes with initially peaked SXR profiles using the SXR maximum - retrieved by tomography - as a proxy. The method has been presented in its key technical details, ranging from improvements of the SXR tomography to the definition of a generalised geometrical displacement. Its robustness was assessed with respect to key aspects like the regularisation or the relation between SXR maximum and the displaced core in a rotating W-contaminated plasma. The philosophy was to make the method transparent and accessible to allow for constructive long-term incremental improvements by the community.

It was shown that both the displacement and its growth rate can be retrieved successfully provided some implicit conditions are met, like profile peakedness or small growth rate compared to the mode frequency and to W thermal velocity. Some quantitative definitions were proposed to allow for characterisation of crash precursors from available experimental data.

The proposed method was applied to 3 typical precursors with different characteristics. All cases display non-constant growth rates, non-monotonicity and piece-wise behaviour. These aspect strongly suggest non-linear growth, the determinants of which remain to be identified.

The frequency of each precursor was shown to be closely related to the bulk plasma rotation and little or no effect of the electron diamagnetic frequency could be evidenced.

It was confirmed that a precursor could be initiated in a fishbone-like manner, thus supporting the idea that fast ions can influence the sawtooth crash onset. Thanks to the interpretation suggested by an MHD simulation, it was also shown that a transient damping of the growth rate can be correlated to a similarly transient competition with a 2/2 mode, thus underlining the role of non-linear interactions between harmonics. A slow crash was empirically related to a smaller $q = 1$ surface - thus suggesting a smaller $1 - q_0$ value - consistently with recent literature. Finally, it was shown that the role of the pressure gradient at $q = 1$ suggested by a simple extrapolation of linear theory was not sufficient to understand crash duration.

Among the limitations of this work, are the small

number of cases studied so far and the unavailability of some experimental data (robusts estimates of q_0 in particular). A systematic study on a larger database, of the order of several tens of cases at least, is currently being carried out to provide more robust observations and help identify reproducible patterns and key plasma parameters in the determination of the onset criterion or the precursor behaviour and lifetime. Additionally, the simulation used to help interpret Case 2 was not completely realistic and more experimentally-relevant simulations are currently being performed.

Acknowledgments

The authors would like to thank Prof. Hartmut Zohm for organizing and leading regular and fruitful interdisciplinary MHD meetings were most of the presented work was discussed in details. This work has been carried out within the framework of the EUROfusion Consortium and has received funding from the Euratom research and training programme 2014-2018 under grant agreement No 633053. The views and opinions expressed herein do not necessarily reflect those of the European Commission. This project was also supported by an EFDA Fellowship for Fusion Research 2014-2016.

Appendix A. Displacement error estimate with no noise and infinite sampling

Given an ellipse-based trajectory, with zero noise and $t_0 = 0$:

$$\begin{cases} R(t) = R_A(t) + r(t)\cos(\theta(t)) \\ Z(t) = Z_A(t) + \zeta r(t)\sin(\theta(t)) \end{cases}$$

$$\begin{cases} r(t) = r_0 e^{\gamma t} \\ \theta(t) = 2\pi f t \end{cases} \quad \begin{cases} R_A(t) = R_{A,0} + V_R t \\ Z_A(t) = Z_{A,0} + V_Z t \end{cases}$$

The 'real' generalised radius at time t is the one associated to the instantaneous ellipse E: $\xi_E = r\sqrt{\zeta}$. The surface computed, assuming infinite time sampling of the trajectory, by the proposed method S is the sum of the integral of the spiral on fraction κ, S_I, plus the triangular surface S_T recovered when taking the convex hull of the polygon, $S = S_I + S_T$, as illustrated in Fig A1.

In the following, we assume that:

(i) The mode frequency does not vary significantly over one period : $\frac{\Delta f}{f}(t) << 1$

(ii) The growth rate does not vary significantly over one period : $\frac{\Delta \gamma}{\gamma}(t) << 1$

(iii) The ellipticity does not vary significantly over one period : $\frac{\Delta \zeta}{\zeta}(t) << 1$

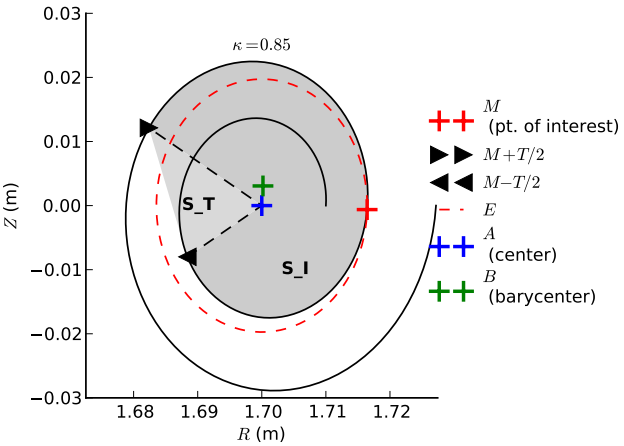

Figure A1: Illustration of the principle used to define a robust displacement from a spiralling trajectory in a surface-based approach taking into account the fact that finite sampling only allows to integrate over a fraction κ of a period. The surface of the remaining triangle is retrieved by taking the convex hull of the polygon (here the polygon is assumed to have infinite sampling).

(iv) The drift speed is very small compared to the trajectory : $r(t) >> \frac{\|v_A\|}{f}(t)$

Under these conditions:

$$\begin{aligned} S_T &= \tfrac{1}{2}\|\underline{AM}_{t+\kappa T/2} \wedge \underline{AM}_{t-\kappa T/2}\| \\ &= \tfrac{1}{2} r_0^2 \zeta e^{2\gamma t}\sin(2\pi f(t-\kappa\tfrac{T}{2}) - 2\pi f(t+\kappa\tfrac{T}{2})) \\ &= \tfrac{1}{2} r_0^2 \zeta e^{2\gamma t}\|\sin(2\pi\kappa)\| \end{aligned}$$

And

$$\begin{aligned} S_I &= \pi \int_{t-\kappa T/2}^{t_i+\kappa T/2} \hat{r}^2(t) f(t) dt \\ &= r_0^2 \pi f \tfrac{1+\zeta^2}{2} \int_{t-\kappa\frac{T}{2}}^{t+\kappa\frac{T}{2}} e^{2\gamma t}\left(1+\cos(2\phi)\cos(4\pi f t)\right) dt \end{aligned}$$

$$\text{If } \begin{cases} \cos(\psi) = \frac{2\gamma}{\sqrt{(2\gamma)^2+(4\pi f_{mode})^2}} \\ \sin(\psi) = \frac{4\pi f_{mode}}{\sqrt{(2\gamma)^2+(4\pi f_{mode})^2}} \end{cases}, \text{ then:}$$

$$\begin{aligned} S_T &= r_0^2 \pi f_{mode} \tfrac{1+\zeta^2}{2} \left(\left[\frac{e^{2\gamma t}}{2\gamma}\right]_{t-\kappa\frac{T}{2}}^{t+\kappa\frac{T}{2}} + \ldots \right. \\ &\left. \frac{\cos(2\phi)}{\sqrt{(2\gamma)^2+(4\pi f)^2}} \left[\cos(4\pi f t - \psi) e^{2\gamma t}\right]_{t-\kappa\frac{T}{2}}^{t_i+\kappa\frac{T}{2}} \right) \\ &= r_0^2 \pi \tfrac{1+\zeta^2}{2} e^{2\gamma t} \kappa \tfrac{\sinh\left(\kappa\frac{\gamma}{f}\right)}{\kappa\frac{\gamma}{f}} \left(1 + \tfrac{1-\zeta^2}{1+\zeta^2} \tfrac{\cos(4\pi f t - \psi + 2\pi\kappa)}{\sqrt{1+\left(\frac{2\pi f}{\gamma}\right)^2}}\right) \end{aligned}$$

Hence, remembering that $r\sqrt{\zeta} = \sqrt{\zeta} r_0 e^{\gamma t}$ and $\xi = \sqrt{\frac{S_T+S_I}{\pi}}$, we can write:

$$\begin{aligned} \frac{\xi}{r\sqrt{\zeta}} &= \left(\tfrac{\|\sin(2\pi\kappa)\|}{2\pi} + \tfrac{\kappa}{2} \tfrac{\sinh\left(\kappa\frac{\gamma}{f}\right)}{\kappa\frac{\gamma}{f}} \times \ldots \right. \\ &\left. \left(\tfrac{1+\zeta^2}{\zeta} + \tfrac{1-\zeta^2}{\zeta} \tfrac{\cos(4\pi f t - \psi + 2\pi\kappa)}{\sqrt{1+\left(\frac{2\pi f}{\gamma}\right)^2}}\right)\right)^{1/2} \end{aligned}$$

Thus, if, as in our case $\kappa \approx 1$, we can write:

$$\frac{\xi}{r\sqrt{\zeta}} = \sqrt{\frac{1}{2}\frac{\sinh\left(\frac{\gamma}{f}\right)}{\frac{\gamma}{f}}\left(\frac{1+\zeta^2}{\zeta} + \frac{1-\zeta^2}{\zeta}\frac{\cos(4\pi f t - \psi)}{\sqrt{1+\left(\frac{2\pi f}{\gamma}\right)^2}}\right)}$$

Then, if $\gamma << f$:

$$\frac{\xi}{r\sqrt{\zeta}} \approx \sqrt{\frac{1+\zeta^2}{2\zeta}}$$

Which is unity for $\zeta = 1$ and 1.12 (i.e. 12% error) for $\zeta = 2$.
If, on the other hand, if $\gamma \approx f$, we have:

$$\begin{aligned}\frac{\xi}{r\sqrt{\zeta}} &\approx 0.767\sqrt{\frac{1+\zeta^2}{\zeta} + \frac{1-\zeta^2}{\zeta}\frac{\cos(4\pi f t-\psi)}{\sqrt{1+4\pi^2}}} \\ &< 0.767\sqrt{\frac{\zeta^2+1}{\zeta} + \frac{\zeta^2-1}{\zeta}\frac{1}{\sqrt{1+4\pi^2}}}\end{aligned}$$

Which is 1.08 for $\zeta = 1$ and 1.27 for $\zeta = 2$. Hence, even with at the limit of validity of our geometrical approach (i.e. $\gamma \approx f$), the error remains reasonable (of the order of 25% with a strongly elongated plasma).

Appendix B. Center of rotation error estimate with no noise and infinite sampling

Additionally, computing the center of mass of surface S (point B in Fig. 7) for each time step yields a proxy of the spiral center (point A in Fig. 7). This proxy is a rough approximation and its own trajectory is also a spiral. Hence, it is possible - to refine the approximation - to perform again the same operation (i.e. to derive the center of mass based on the trajectory of B). This operation can be performed iteratively and gets more accurate each time. The error with respect to A, for the N-th iteration, scales as $\left(\frac{\gamma}{f}\right)^N$ when $\frac{\gamma}{f} \ll 1$ (cf. Appendix B). We use this approximation at the 3rd order.

For simplification of the calculations we assume here that $\kappa = 1$ and that we are dealing with a circular spiral $\zeta = 1$ with a fixed center. Then, if B is the center of mass of the surface spanned over one period:

$$\begin{aligned}\underline{OB} &= \begin{pmatrix} x_A + \frac{2\pi f}{S_i}\int_{t-T/2}^{t+T/2}\int_0^{r_0 e^{\gamma t}} r^2 dr\cos(2\pi f t)\,dt \\ y_A + \frac{2\pi f}{S_i}\int_{t-T/2}^{t+T/2}\int_0^{r_0 e^{\gamma t}} r^2 dr\sin(2\pi f t)\,dt \end{pmatrix} \\ &= \begin{pmatrix} x_A + r\frac{2}{3C\pi}\frac{\gamma}{f}\frac{\sinh(\frac{3\gamma}{2f})}{\sinh(\frac{\gamma}{f})}\cos(2\pi f t_i - (\phi-\pi)) \\ y_A + r\frac{2}{3C\pi}\frac{\gamma}{f}\frac{\sinh(\frac{3\gamma}{2f})}{\sinh(\frac{\gamma}{f})}\sin(2\pi f t_i - (\phi-\pi)) \end{pmatrix}\end{aligned}$$

With

$$\begin{cases} \frac{\frac{3\gamma}{2\pi f}}{C} = \cos(\phi) \\ \frac{1}{C} = \sin(\phi) \\ C = \sqrt{1+\left(\frac{3\gamma}{2\pi f}\right)^2} \end{cases}$$

Hence, if r_B is the radius of the center of mass B then:

$$\frac{r_B}{r} = \frac{2}{3C\pi}\frac{\gamma}{f}\frac{\sinh(\frac{3\gamma}{2f})}{\sinh(\frac{\gamma}{f})}$$

The trajectory of B is thus also a spiral, of the same frequency as the mode itself, but a radius decreased by a constant factor. Re-iterating the same operation on the trajectory of B will yield another spiral, with a radius reduced again by the same factor. More generally, at the N-th order, the radius is:

$$\frac{r_B^N}{r} = \left(\frac{2}{3C\pi}\frac{\gamma}{f}\frac{\sinh(\frac{3\gamma}{2f})}{\sinh(\frac{\gamma}{f})}\right)^N$$

Which scales as $\left(\frac{\gamma}{f}\right)^N$ when $\frac{\gamma}{f} << 1$. Thus, if $\frac{\gamma}{f}$ is small, the center of mass of the surface spanned by one period, computed at the N-th order, is a good approximation of the real center of the spiral. Numerically we use the 3rd order to get satisfactory results (error less than 1 mm).

Appendix C. Kadomtsev-based crash times

The crash times estimated from Kadomtsev-based models (the varying part is the content of Ohm's law) give the order of magitude of the duration of the total magnetic reconnection. Experimentally, we see that the reconnection process can be divided into phases with varying growth rates. Each phase i can be identified and characterised by a duration Δt_i and a displacement $\Delta\xi_i$. Let us calculate the time this partial reconnection should take with a similar approach as the one used for Kadomtsev-derived crash times. The equation of mass conservation from the inflow to the outflow yields:

$$r_1 v_{in} = \delta v_{out}$$

where δ is the thickness of the resistive layer, v_{in} is an estimate of the core velocity (influx velocity), v_{out} is the outflow velocity and r_1 is an estimate of the $q = 1$ radius which is itself an estimate of the length on which the reconnection happens. Then, from volumic energy conservation, we derive an estimate of the outflow velocity as the reconnected flux Alfven time:

$$\frac{B_\theta^{*2}}{2\mu_0} = \frac{\rho v_{out}^2}{2} \Rightarrow v_{out} = \frac{B_\theta^*}{\sqrt{\mu_0\rho}} = v_A^*$$

Where $B_\theta^* \approx (1-q_0)B_\theta$ is the reconnected part of the poloidal magnetic field. Then, the time necessary for displacement $\Delta\xi_i$ is approximately:

$$\Delta t_i = \frac{\Delta\xi_i}{v_{in}} = \Delta\xi_i \frac{r_1}{\delta v_A^*}$$

So the outflow velocity is fixed by the reconnected flux, the only changeable part is the width δ of the resistive layer. It is derived from a combination of Faraday's law and Ohm's law [10, 61, 11]:

$$\begin{cases} E - v_{in}B_\theta^* = 0 \\ E = \eta j + \frac{m_e}{n_e e^2}\frac{v_{in}}{\delta} j + \frac{m_e}{n_e e^2}\frac{v_{T_e}}{L} j \end{cases}$$

where the first term on the right hand side is due to the plasma resistivity [10], the second term is the electron inertia [61] and the last term corresponds to the electron parallel viscosity [11]. With n_e, m_e and e the electron density, mass and charge, η the plasma resistivity, j the current density, $v_{T_e} = \sqrt{\frac{k_B T_e}{m_e}}$ the electron thermal velocity and $L \approx r_1 \frac{B}{B_\theta^*}$ the acceleration length of electrons.

If we consider that the dominant term is the plasma resistivity, we retrieve a sligthly modified version of the original Kadomtsev time scale by introducing the resistive diffusion time scale $\tau_{RD} = \frac{r_1^2 \mu_0}{\eta}$ and the reconnected flux Alfven time scale $\tau_A^* = \frac{r_1}{v_A^*}$:

$$\delta = \sqrt{\frac{\eta r_1}{\mu_0 v_A^*}} \Rightarrow \Delta t_i = \frac{\Delta\xi_i}{r_1}\sqrt{\tau_{RD}\tau_A^*}$$

If the resistive layer width is controlled by electron inertia then, introducing the plasma pulsation $\omega_P = \sqrt{\frac{n_e e^2}{\epsilon_0 m_e}}$:

$$\delta = \sqrt{\frac{m_e}{\mu_0 n_e e^2}} = \frac{c}{\omega_P} \Rightarrow \Delta t_i = \frac{\Delta\xi_i}{r_1}\frac{r_1\omega_P}{c}\tau_A^*$$

And if the electron parallel viscosity is dominant then:

$$\delta = \sqrt{\frac{1}{\tau_A^*}\frac{c^2}{\omega_P^2}\frac{v_{T_e}}{L}} \Rightarrow \Delta t_i = \frac{\Delta\xi_i}{r_1}\frac{r_1\omega_P}{c}\sqrt{\frac{\tau_A^* L}{v_{T_e}}}$$

In order to compare the experimental time scale in each growth phase with the same reference time scales, we simply compare $\Delta t_i \frac{r_1}{\Delta\xi_i}$ to $\tau_{K,\eta} = \sqrt{\tau_{RD}\tau_A^*}$, $\tau_{K,e} = \frac{r_1\omega_P}{c}\tau_A^*$ and $\tau_{K,v} = \frac{r_1\omega_P}{c}\sqrt{\frac{\tau_A^* L}{v_{T_e}}}$.

References

[1] S. von Goeler, W. Stodiek, and N. Sauthoff, "Studies of internal disruptions and m=1 oscillations in tokamak discharges with soft x-ray techniques," *Physical Review Letters*, vol. 33, no. 20, p. 1201, 1974.

[2] C. P. Tanzi and H. J. de Blank, "New method to analyze internal disruptions with tomographic reconstructions," *Physics of Plasmas*, vol. 4, no. 3, p. 696, 1996.

[3] F. Porcelli, D. Boucher and M. N. Rosenbluth, "Model for the sawtooth period and amplitude," *Plasma Physics and Controlled Fusion*, vol. 38, p. 2163, 1996.

[4] O. Sauter *et al.*, "Control of neoclassical tearing modes by sawtooth control," *Physical Review Letters*, vol. 88, no. 10, p. 105001, 2002.

[5] T. C. Hender *et al.*, "Chapter 3: MHD stability, operational limits and disruptions," *Nuclear Fusion*, vol. 47, p. 128, 2007.

[6] V. Igochine *et al.*, "Destabilization of fast particle stabilized sawteeth in ASDEX Upgrade with elecron cyclotron current drive," *Plasma Physics and Controlled Fusion*, vol. 53, p. 022002, 2001.

[7] A. W. Edwards *et al.*, "Rapid collapse of a plasma sawtooth oscillation in the JET tokamak," *Physical Review Letters*, vol. 57, no. 2, p. 210, 1986.

[8] J. A. Wesson, A. W. Edwards, and R. Granetz, "Spontaneous m=1 instability in the JET sawtooth collapse," *Nuclear Fusion*, vol. 31, no. 1, p. 111, 1991.

[9] H. R. Koslowski, H. Soltwisch, and W. Stodiek, "Polarimetric measurement of m=1 sawtooth precursor oscillations in the TEXTOR tokamak," *Plasma Physics and Controlled Fusion*, vol. 38, p. 271, 1996.

[10] B. B. Kadomtsev *Soviet Journal of Plasma Physics*, vol. 1, p. 389, 1975.

[11] Q. Yu, "A new theoretical model for fast sawtooth collapse," *Nuclear Fusion*, vol. 35, no. 8, p. 1012, 1995.

[12] Q. Yu, S. Guenter and K. Lackner, "Formation of plasmoids during sawtooth crashes," *Nuclear Fusion*, vol. 54, p. 072005, 2014.

[13] V. Igochine *et al.*, "Stochastic sawtooth reconnection in ASDEX Upgrade," *Nuclear Fusion*, vol. 47, p. 23, 2007.

[14] V. Igochine, O. Dumbrajs, H. Zohm and the ASDEX Upgrade Team, "Transition from quasiperiodicity to chaos just before sawtooth crash in the ASDEX Upgrade tokamak," *Nuclear Fusion*, vol. 48, p. 062001, 2008.

[15] V. Igochine *et al.*, "Structure and dynamics of sawteeth crashes in ASDEX Upgrade," *Physics of Plasmas*, vol. 17, p. 122506, 2010.

[16] J. F. Drake and R. G. Kleva, "Collisionless reconnection and the sawtooth crash," *Physical Review Letters*, vol. 66, no. 11, p. 1458, 1991.

[17] D. Vezinet, V. Igochine, A. Gude, and D. Meshcheriakov, "Experimental characterisation of sawtooth crash precursors on ASDEX Upgrade via Soft X-Ray tomography," *proc. 42nd EPS conf. plasm. phys.*, 2015. P1.138.

[18] M. Yamada *et al.*, "Investigation of magnetic reconnection during a sawtooth crash in a high-temperature tokamak plasma," *Physics of Plasmas*, vol. 1, no. 10, p. 3269, 1994.

[19] Y. Nagayama *et al.*, "Analysis od sawtooth oscillations using simultaneous measurements of electron cyclotron emission imaging and x-ray tomography on tftr," *Physical Review Letters*, vol. 67, no. 25, p. 3527, 1991.

[20] A. Letsch *et al.*, "Incomplete reconnection in sawtooth crashes in ASDEX Upgrade," *Nuclear Fusion*, vol. 42, p. 1055, 2002.

[21] M. Sertoli, "Characterisation of saturated MHD instabilities through 2d electron temperature profile reconstruction from 1d ece measurements," *Nuclear Fusion*, vol. 53, p. 053015, 2013.

[22] H. K. Park *et al.*, "Observation of high-field-side crash and heat transfert during sawtooth oscillation in magnetically confined plasmas," *Physical Review Letters*, vol. 96, p. 195003, 2006.

[23] H. K. Park *et al.*, "New insights to the sawtooth oscillation ('m/n=1/1 mode') in hot plasmas based on high

resolution 2-d images of te fluctuations," *Plasma and Fusion Research*, vol. 2, p. 1002, 2007.

[24] T. Nicolas, R. Sabot, X. Garbet, H. Lütjens, J.-F. Luciani, A. Sirinelli, J. Decker, and A. Merle, "Particle flow during sawtooth reconnection: Numerical simulations of experimental observations," *Plasma and Fusion Research*, vol. 8, no. 0, pp. 2402131–2402131, 2013.

[25] H. Soltwisch, "Measurement of current-density changes during sawtooth activity in a tokamak by far-infrared polarimetry," *Review of Scientific Instruments*, vol. 59, no. 8, p. 1599, 1988.

[26] M. Schittenhelm, H. Zohm and the ASDEX Upgrade Team, "Analysis of coupled MHD modes with mirnov probes in ASDEX Upgrade," *Nuclear Fusion*, vol. 37, no. 9, p. 1255, 1997.

[27] J. S. Kim *et al.*, "MHD mode identification of tokamak plasmas from mirnov signals," *Plasma Physics and Controlled Fusion*, vol. 41, p. 1399, 1999.

[28] V. Igochine *et al.*, "Active control of magneto-hydrodynamic instabilities in hot plasmas," in *Springer Series*, vol. 83, ch. 3, pp. 53–104, first ed., 2015.

[29] T. Puetterich *et al.*, "Calculation and experimental test of the cooling factor of tungsten," *Nuclear Fusion*, vol. 50, no. 2, p. 025012, 2010.

[30] F. L. Hinton and S. K. Wong, "Neoclassical ion transport in rotating axisymmetric plasmas," *Physics of Fluids*, vol. 28, p. 3082, 1985.

[31] J. A. Wesson, "Poloidal distribution of impurities in a rotating tokamak plasma," *Nuclear Fusion*, vol. 37, no. 5, p. 577, 1997.

[32] L. Ingesson, H. Chen, P. Helander and M. J. Mantsinen, "Comparison of basis functions in soft x-ray tomography and observation of poloidal asymetries in impurity density," *Plasma Physics and Controlled Fusion*, vol. 42, no. 2, p. 161, 2000.

[33] H. Chen *et al.*, "Poloidally asymmetric distribution of impurities in joint european torus plasmas," *Physics of Plasmas*, vol. 7, no. 11, p. 4567, 2000.

[34] M. L. Reinke *et al.*, "Poloidal variation of high-z impurity density due to hydrogen minority ion cyclotron resonance heating on Alcator C-Mod," *Plasma Physics and Controlled Fusion*, vol. 54, no. 4, p. 045004, 2012.

[35] V. Igochine, A. Gude, M. Maraschek and ASDEX Upgrade Team, "Hotlink based soft x-ray diagnostic on ASDEX Upgrade," 2010. Technical Report IPP 1/338, Max-Planck-Institut fuer Plasmaphysik, Garching(DE).

[36] M. Weiland *et al.*, "Investigation of 3D tungsten distributions in (1,1) kink modes induced by toroidal plasma rotation," *Plasma Physics and Controled Fusion*, vol. 57, p. 085002, 2015.

[37] P. C. Hansen, "Numerical tools for analysis and solution of fredholm integral equations of the first kind," *Inverse problems*, vol. 8, no. 6, p. 849, 1999.

[38] L. C. Ingesson, H. Chen, P. Helander and M. J. Mantsinen, "Comparison of basis functions in soft x-ray tomography and observation of poloidal asymmetries in impurity density," *Plasma Physics and Controlled Fusion*, vol. 42, no. 2, p. 161, 1999.

[39] L. C. Ingesson *et al.*, "Projection-space methods to take into account finite beam-width effects in two-dimensional tomography algorithms," *Journal of the Optical Society of America A*, vol. 16, no. 1, p. 17, 1999.

[40] A. N. Tikhonov, "Solution of incorrectly formulated problems and regularization method," *Doklady Akademy Nauk SSSR*, vol. 151, no. 3, p. 501, 1963.

[41] A. N. Tikhonov, "Regularization of incorrectly posed problems," *Doklady Akademy Nauk SSSR*, vol. 153, no. 1, p. 49, 1963.

[42] M. Hanke, "Limitations of the l-curve method in ill-posed problems," *BIT Numerical Mathematics*, vol. 36, no. 2, p. 287, 1996.

[43] G. C. Fehmers, L. P. J. Kamp and F. W. Sluijter, "An algorithm for quadratic optimization with one quadratic constraint and bounds on the variables," *Inverse problems*, vol. 14, no. 4, p. 893, 1999.

[44] M. Anton *et al.*, "X-ray tomography on the tcv tokamak," *Plasma physics and controlled fusion*, vol. 8, p. 1849, 1996.

[45] L. C. Ingesson *et al.*, "Soft x ray tomography during elms and impurity injection in JET," *Nuclear Fusion*, vol. 38, no. 11, p. 1675, 1998.

[46] L. C. Ingesson, B. Alper, B. J. Peterson and J. C. Vallet, "Tomography diagnostics: bolometry and soft x-ray detection," *Fusion Science and Technology*, vol. 53, no. 2, p. 528, 2008.

[47] D. Vezinet, *Soft x-ray measurement and analysis on tokamaks in view of real-time control.* PhD thesis, Aix-Marseille University, CEA-IRFM, 13108 Saint Paul-lez-Durance, 2013.

[48] D. Vezinet and A. Ratnani, "Tofu : a python library for advance tomography on fusion devices." to be submitted to Review of Scientific Instruments.

[49] J. C. Fuchs, F. Mast, A. Herrmann and K. Lackner, "Two dimensional reconstruction of the radiation power density in ASDEX Upgrade," *presented at the 21st EPS Conference on Plasma Physics*, vol. 18B, p. 1308, 1994.

[50] M. Odstrcil, J. Mlynar, B. Alper and A. Murari, "Modern numerical methods for plasma tomography optimisation," *Nuclear Instruments and Methods in Physics Research Section A: Accelerators, Spectrometers, Detectors and Associated Equipment*, vol. 686, p. 156, 2012.

[51] F. Porcelli, E. Rossi, G. Cima and A. Wootton, "Macroscopic magnetic islands and plasma energy transport," *Physical Review Letters*, vol. 82, p. 1458, 1999.

[52] V. S. Udintsev *et al.*, "Experimental observation of m/n=1/1 mode behaviour during sawtooth activity and its manifestations in tokamak plasmas," *Plasma Physics and Controlled Fusion*, vol. 47, p. 1111, 2005.

[53] P. Lauber *et al.*, "Kinetic alfvn eigenmodes at ASDEX Upgrade," *Plasma Physics and Controlled Fusion*, vol. 51, no. 12, p. 124009, 2009.

[54] J. A. Wesson, *Tokamaks.* CLARENDON PRESS-OXFORD, third ed., 2004.

[55] K. McGuire *et al.*, "Study of high-beta magnetohydrodynamic modes and fast-ion losses in pdx," *Physical Review Letters*, vol. 50, p. 891, 1983.

[56] H. Zohm, *Magnetohydrodynamic Stability of Tokamaks.* Wiley-VCH Verlag GmbH and Co. KGaA., first ed., 2015.

[57] M. F. F. Nave *et al.*, "Fishbone activity in JET," *Nuclear Fusion*, vol. 31, no. 4, p. 697, 1991.

[58] S. Guenter *et al.*, "The influence of the fishbones on the background plasma," *Nuclear Fusion*, vol. 39, p. 1535, 1999.

[59] V. Igochine *et al.*, "Active control of magneto-hydrodynamic instabilities in hot plasmas," in *Springer Series*, vol. 83, ch. 4, pp. 105–142, first ed., 2015.

[60] Q. Yu, S. Guenter and K. Lackner, "Numerical modelling of sawtooth crash using two-fluid equations," *Nuclear Fusion*, vol. 55, p. 113008, 2015.

[61] J. A. Wesson, "Sawtooth reconnection," *Nuclear Fusion*, vol. 30, no. 12, p. 2545, 1990.